JOURNAL OF GEOPHYSICAL RESEARCH, VOL. 113, B06405, doi:10.1029/2006JB004811, 2008

Dynamics of Mount Etna before, during, and after the July–August 2001 eruption inferred from GPS and differential synthetic aperture radar interferometry data

Giuseppe Puglisi,[1] Alessandro Bonforte,[1] Alessandro Ferretti,[2] Francesco Guglielmino,[1] Mimmo Palano,[1] and Claudio Prati[3]

Received 19 October 2006; revised 10 November 2007; accepted 21 February 2008; published 20 June 2008.

[1] Ground deformation data from GPS and differential synthetic aperture radar interferometry (DInSAR) techniques are analyzed to study the July–August 2001 Mount Etna eruption as well as the dynamics preceding and following this event. Five GPS surveys were carried out on the entire Mount Etna network or on its southeastern part, from July 2000 to October 2001. Five ERS-2 ascending passes and three descending ones are used to form five interferograms spanning periods from a month to 1 year, before and encompassing the eruption. Numerical and analytical inversions of the GPS and DInSAR data were performed to obtain analytical models for preeruptive, syneruptive and posteruptive periods. The deformation sources obtained were from the Mogi model: (1) pressure sources located beneath the upper western flank of the volcano, inflating before the eruption onset and deflating afterward; (2) tensile dislocations to model the intrusion of a N-S dike in the central part of the volcano; and (3) two sliding and two normal dislocations to model the eastern and southern flank dynamics. This study confirms that the lower vents of the eruption were fed by a magma stored at depth ranging from 9 to 4 km below sea level, as proposed from petrochemical and geophysical researches. The rising of the magma through the shallow crust started months before the eruption onset but accelerated on the last day; this study suggests that in the volcanic pile the path of the rising magma was driven by the volcano topography. The eastern sliding plane and the interaction between dike intrusion and flank instability have been better defined with respect to previous studies. The sliding motion abruptly accelerated with the dike intrusion, and this continued after the end of the eruption. The acceleration was accompanied by the propagation of the strain field toward the eastern periphery of the volcano.

Citation: Puglisi, G., A. Bonforte, A. Ferretti, F. Guglielmino, M. Palano, and C. Prati (2008), Dynamics of Mount Etna before, during, and after the July–August 2001 eruption inferred from GPS and differential synthetic aperture radar interferometry data, *J. Geophys. Res.*, *113*, B06405, doi:10.1029/2006JB004811.

1. Introduction

[2] The geodynamic framework of Mount Etna is characterized by a compressive stress regime, trending roughly N-S, due to the Eurasia-Africa plate collision, and an extensional regime trending roughly E-W, related to the oceanic Ionian domain consumption (see *Bousquet and Lanzafame* [2004] for an overall review). Two regional tectonic features cut the unbuttressed eastern side of the volcano: the NNW-SSE striking Timpe fault system (TFS) and the Piedimonte fault (Figure 1). They are considered as the onshore prolongation of the Hybleo-Maltese escarpment (Figure 1) and as part of the NE-SW Messina-Etna system [*Lanzafame et al.*, 1996; *Azzaro*, 1999], respectively. The eastern flank of the volcanic edifice shows an eastward movement. Many studies have argued that this continuous ESE seaward sliding is due to the interrelationship between gravity instability and magma intrusion [e.g., *Borgia et al.*, 1992; *Lo Giudice and Rasà*, 1992; *Rust and Neri*, 1996; *Bonforte and Puglisi*, 2003; *Rust et al.*, 2005]. Although the published models propose different explanations of the origin of the flank movement, they all agree on identifying the Pernicana fault system (Figure 1) as the northern boundary of the unstable sector. The southern part of the western boundary of the sector is represented by the South Rift [*Rasà et al.*, 1996] joining, southeastward, with the Mascalucia-Tremestieri-Trecastagni fault system (Figure 1). This fault system is made up of a number of NNW-SSE striking faults showing evident right-lateral displacement and is also characterized by very shallow seismicity, with typical focal depths of 1–2 km. The high geodynamic activity of this sector of Mount Etna is testified by its

[1] Istituto Nazionale di Geofisica e Vulcanologia, Catania, Italy.
[2] Tele-Rilevamento Europa, Milan, Italy.
[3] Dipartimento di Elettronica e Informazione, Politecnico di Milano, Milan, Italy.

0148-0227/08/2006JB004811$09.00

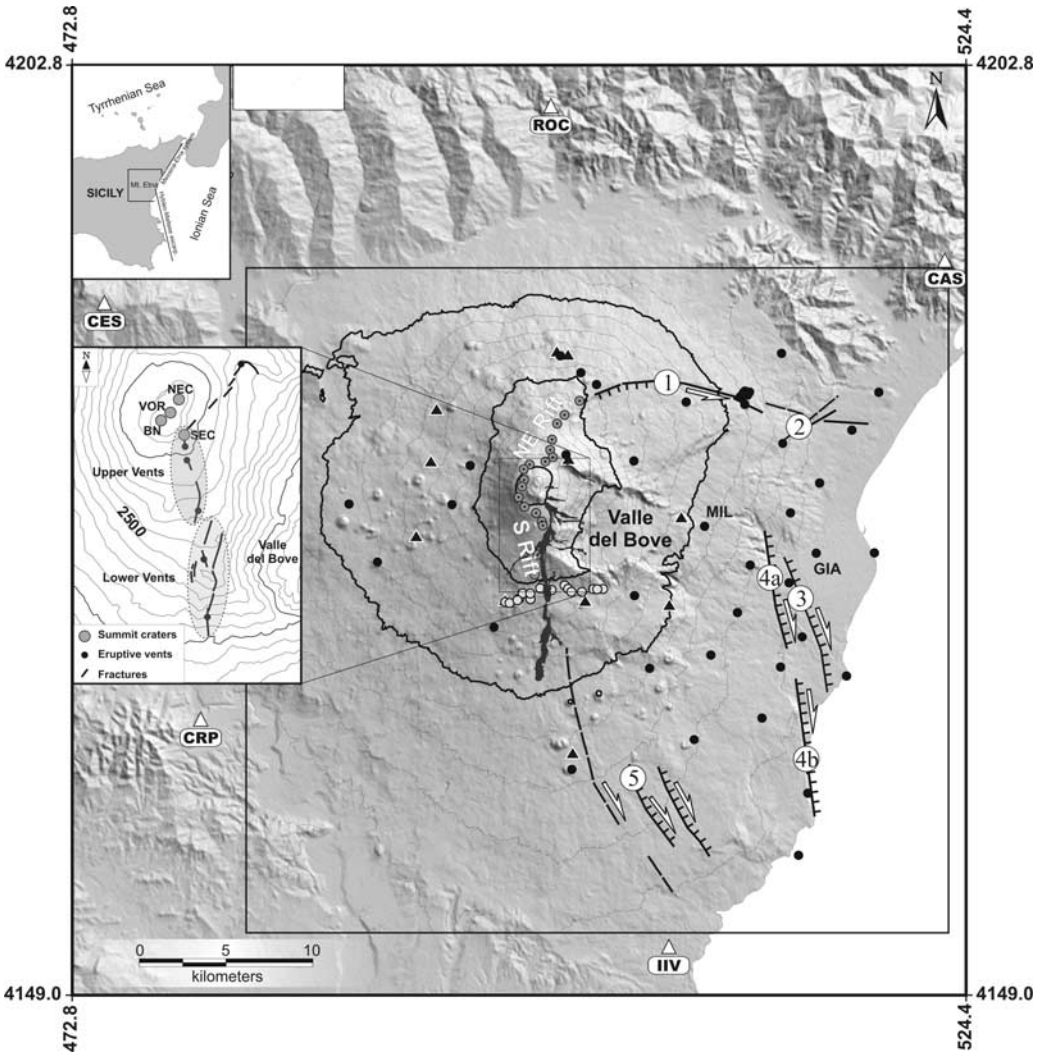

Figure 1. Sketch map of Mount Etna showing the structures discussed in the paper: 1, Pernicana fault; 2, Piedimonte fault; 3, San Leonardello fault (SLF in text and Figure 8); 4, Timpe fault system (TFS in text and Figure 8) (a, Moscarello fault; b, Acireale fault [*Azzaro*, 1999]); 5, Mascalucia-Tremestieri-Trecastagni faults system. Bars indicate the downthrown side, and arrows indicate the major strike-slip components for each fault. The 2001 lava flows (southern flank) are drawn in black. Mount Etna GPS Network is also reported: white triangles indicate the ''External Reference Frame'' benchmarks; black points indicate the ''Inner'' and ''Ionica'' network benchmarks; gray points indicate the ''North-South Kinematic Profile'' benchmarks; white points indicate the ''East-West Kinematic Profile'' benchmarks; black triangles indicate the ''Permanent GPS'' stations. The box indicates the area shown in Figures 3, 4, 5, 6, and 7. The inset details the area of the summit craters and the fissure systems (inset redrawn from *Acocella and Neri* [2003]). Coordinates are in UTM projection, zone 33N.

greater seismicity, with respect to the rest of the volcano [*Gresta et al.*, 1990].

[3] Other important results obtained during recent decades, mainly due to the vast improvement in the seismic and deformation monitoring networks, are the identification of the main structural features and the paths along which the magma rises beneath Mount Etna. Seismic tomographies define the basement of Mount Etna as characterized by a main upper and middle crustal intrusion complex, with high V_P values, (High Velocity Body; HVB) whose top is located at about 4 km below sea level (bsl), beneath the southern-eastern flank of Mount Etna (see *Chiarabba et al.* [2004] for a review). During recent decades magma ascended along the western boundary of the HVB, as confirmed by ground deformation and seismic studies [e.g., *Patanè et al.*, 2003; *Puglisi et al.*, 2004, and references therein]. It is noteworthy that the absence of evidence of large magmatic storage volumes strongly supports the idea that, during its ascent along the western boundary of the HVB, the magma could be stored as a plexus of dikes or sills, as suggested by *Armienti et al.* [1989] to justify the typical polybaric evolution of the magmas within the plumbing system of Mount Etna [*Corsaro and Pompilio*, 2004].

[4] The 2001 eruption was the first lateral eruption after the 1991–1993 one. From 1993, a continuous inflation of the volcano with an almost constant rate was recorded

[*Puglisi and Bonforte*, 2004] and the whole eastern flank of the volcano underwent a continuous, seaward motion. This movement was detected by differential synthetic aperture radar interferometry (DInSAR) [*Froger et al.*, 2001] and GPS data and modeled as a large-scale sliding of the volcanic pile together with the upper part of the sedimentary substratum [*Bonforte and Puglisi*, 2003, 2006; *Palano et al.*, 2007; *Puglisi and Bonforte*, 2004].

[5] In this paper, we analyze the ground deformation preceding, accompanying and following the July–August 2001 flank eruption that represents the first important intrusion on Mount Etna to be investigated by a dense and wide GPS monitoring array and by the DInSAR technique. Furthermore, the available GPS and DInSAR data sets allow the relationship between dike intrusions and volcano flank instability to be investigated.

2. The 2001 Mount Etna Eruption

[6] The lateral July–August 2001 eruption on Mount Etna was heralded by an intense seismic swarm starting on the night of 12 July [*INGV Staff*, 2001; *Patanè et al.*, 2002]. More than 2600 seismic shocks (M_{MAX} = 3.9) occurred in less than 4 d. The earthquake hypocenters were fairly shallow (1–3 km bsl) and marked the upward propagation of a magmatic dike. This led, between 17 and 20 July, to the formation of two different fissure systems, together forming a 7-km-long fissure field, striking roughly N-S, opened on the middle-upper southern flank (Figure 1). The first fissure system opened on 17 July from 2950 m down to 2700 m above sea level (asl) and was called Upper Vents (UV) [*INGV Staff*, 2001] (Figure 1). The lowest eruptive fissure opened at 2100 m asl on 18 July, producing Strombolian activity and lava flows that expanded toward the south. In the late afternoon of 19 July, two coalescent pit craters opened at 2550 m asl, on the upper southern flank, giving rise to hydromagmatic explosions [*Taddeucci et al.*, 2002] and a thick, dark gray ash cloud. These vents of 18 and 19 July were called the Lower Vents (LV) [*INGV Staff*, 2001] (Figure 1). On 25 July, the activity at 2550 m became magmatic, and the fallout around the pits formed a cinder cone. From the end of July, the lava flows from the UV gradually stopped. The eruption ended at LV on 9 August 2001. Petrologic studies proved that the magma erupted from the LV is more primitive than that emitted from UV, suggesting that the two fissure systems were fed by different magmas [*Métrich et al.*, 2004; *Corsaro et al.*, 2006]. The lava emitted, in terms of Dense Rock Equivalent (DRE), is estimated between 5 and 12 $\times$ 10^6 m^3, for the UV, and 20–25 $\times$ 10^6 m^3, for the LV [*Behncke and Neri*, 2003; *Coltelli et al.*, 2007]. Assuming that the tephra produced by LV is in the order of 5–10 $\times$ 10^6 m^3 [*Coltelli et al.*, 2001], corresponding to about 2–5 $\times$ 10^6 m^3 of DRE [*Behncke and Neri*, 2003], the total volume of magma emitted from LV is about 22–30 $\times$ 10^6 m^3.

3. GPS Surveys and Data Processing

[7] In order to study the dynamics of Mount Etna before, during and after the eruption, data collected from five GPS measurements carried out on Mount Etna networks between July 2000 and October 2001, are analyzed. Furthermore, during the eruption, monitoring was performed frequently by GPS surveys of selected benchmarks crossing the southern end of the fracture system [*Bonforte et al.*, 2004].

[8] The first survey considered (hereafter the Etna 2000 survey) was carried out over the whole Mount Etna GPS network (Figure 1 and Table 1). This network consists of 46 benchmarks organized in three subnetworks: the "External Reference Frame", the "Inner Network", and the "North-South Kinematic Profile" (Figure 1). Detailed descriptions of these GPS networks are reported by *Puglisi et al.* [2004].

[9] After a seismic crisis affecting the southeastern flank of the volcano in January 2001 [*Alparone and Gambino*, 2003], 15 benchmarks selected in the southern part of the "Ionica" GPS network were surveyed (hereafter the Ionica 2001-A survey) (Table 1) [*Bonforte and Puglisi*, 2006] (Figure 1). Four stations (IIV, GIA, MIL, and CAS) belonging to the Etna 2000 survey were included in this survey to allow comparisons with the others (Figure 1).

[10] In June 2001, a major effort was made to build an integrated Mount Etna GPS network that included the "Ionica" and a small GPS network located on the eastern part of the Pernicana fault, in the Rocca Campana area [*Azzaro et al.*, 2001]. The stations of the GPS permanent network implemented during the 2001 spring [*Bonaccorso et al.*, 2004] were also included in this survey (hereafter the Etna 2001-A survey; Table 1). Thus the new network consists of about 70 stations, surveyed by static and kinematic techniques, covering the entire volcano with great spatial detail on its upper and eastern sectors (Figure 1). This campaign ended on 11 July, just a day before the beginning of the seismic swarm accompanying the dike intrusion.

[11] On 17 July, GPS measurements were carried out in kinematic mode on the southern half of the N-S profile to quantify the ground deformations associated with the fracture system forming on the upper southern flank of the volcano during the seismic swarm. After the vent opening, on 18 July, repeated kinematic surveys along an E-W profile located very close to the lowest eruptive vent were performed throughout the eruption to monitor the possible downward propagation of the eruptive fracture [*Bonforte et al.*, 2004]. This profile was integrated in the survey performed in September when the same GPS network measured in June–July (with the exception of the benchmarks destroyed during the eruption) was completely remeasured (hereafter the Etna 2001-B survey) (Table 1).

[12] In late October 2001, a seismic swarm, occurring on the lower eastern flank of the volcano [*Azzaro et al.*, 2002] prompted carrying out a new GPS survey (hereafter the Ionica 2001-B survey) on the same benchmarks as the Ionica 2001-A (Table 1).

[13] All the above surveys were carried out through Trimble double-frequency receivers (4000 SSE, 4000 SSI, and 4700 models), equipped with Compact L1/L2 and Microcentered L1/L2, both with ground planes, and Choke Ring antennas.

[14] Data from each survey are processed using the Trimble Geomatics Office software, version 1.5, according to a procedure established for the previous Mount Etna surveys [*Puglisi et al.*, 2004]. IGS antenna calibration models were introduced to avoid errors deriving from the modeling of the electromagnetic characteristics for different

Table 1. Code, UTM Coordinates, Height, and Measurements for Each Benchmark of Mount Etna GPS Networks[a]

				Surveys				
Code	Longitude	Latitude	Height (m)	ETNA 2000	IONICA 2001-A	ETNA 2001-A	ETNA 2001-B	IONICA 2001-B
BAG1	514170	4172805	280			●	●	●
BAGL	514207	4172754	278		●	●		
CAP	494784	4177299	1922	●		●	●	
CAS	523288	4191439	842	●	●	●	●	●
CES	474742	4188986	1247	●		●	●	
CIS	500633	4175479	2682	●		●		
CIT	505241	4179808	1781	●		●	●	
CRI	508250	4183203	1385	●		●	●	
CRP	480290	4164968	340	●		●	●	
EFAR	507276	4171591	1059			●	●	●
EGDF	501508	4185865	1722			●	●	
EMAL	493939	4182689	1551			●	●	●
EMEG	493585	4179668	1615			●	●	●
EMFN	507941	4176492	1205			●	●	●
EMGL	492816	4175439	1611			●	●	
EPLU	498743	4179754	2965	●		●	●	
ERDV	501886	4179565	2828			●	●	●
ESLN	497777	4171760	1775	●		●	●	●
ETDF	500072	4176712	2969	●		●	●	●
FOPE	506145	4167883	853		●	●	●	●
GIA	515723	4174501	164	●	●	●	●	●
GONA	517774	4181581	94			●	●	
IIV	507254	4151854	89	●	●	●	●	●
ISLA	514706	4157124	67		●	●	●	●
K000	497897	4171716	1773				●	
K003	498134	4171672	1774				●	
K005	498678	4171908	1810				●	
K006	499335	4171891	1853				●	
K007	498882	4172222	1895				●	
K008	499324	4172215	1924				●	
K009	499889	4172514	1942				●	
K010	500541	4172417	1933				●	
K011	501300	4172681	1877				●	
K012	501494	4172482	1823				●	
K013	502287	4172301	1727				●	
K015	502928	4172468	1670				●	
K016	503500	4172479	1613				●	
K04N	503500	4171827	1800				●	
K12B	501677	4172309	1782				●	
K16N	503163	4172460	1647				●	
L23	503093	4184205	1955	●		●	●	
LAM	501013	4185857	1751	●		●	●	
MANG	514919	4169690	211		●	●	●	●
MDGR	515243	4160700	124		●	●	●	●
MIL	509309	4176053	922	●	●	●	●	●
MOSC	511928	4173822	508		●	●	●	●
MPL	501671	4162063	796	●	●	●	●	●
MTSE	508703	4163780	489		●	●	●	●
NICO	501734	4162974	771			●	●	●
NS01	502151	4183270	2134	●		●	●	
NS02	501282	4182458	2358	●		●	●	
NS03	500860	4181959	2456	●		●	●	
NS04	500616	4181603	2538	●		●		
NS05	500574	4181049	2657	●		●	●	
NS06	500461	4180450	2767	●		●	●	
NS07	500609	4180035	2850	●		●	●	
NS08	500187	4179784	2936	●		●	●	
NS09	499284	4179618	3006	●		●	●	
NS10	498964	4178737	3024	●		●	●	
NS11	498964	4178737	3140	●		●	●	
NS16	499984	4176346	2862	●		●	●	
NS17	500042	4176115	2799	●		●	●	
NS18	500386	4175474	2690	●		●		
NS19	499960	4174705	2554	●				
NS20	499759	4174443	2477	●		●		
NS21	499579	4173308	2176	●		●	●	
NS22	500010	4172670	1973	●		●		
NUN	495831	4179544	1830	●		●	●	
OBS	501342	4180163	2820	●				
OSV	501476	4179830	2867	●		●	●	
PAR	497201	4170246	1552	●		●	●	

Table 1. (continued)

				Surveys				
Code	Longitude	Latitude	Height (m)	ETNA 2000	IONICA 2001-A	ETNA 2001-A	ETNA 2001-B	IONICA 2001-B
PDAP	512604	4165017	319		•	•	•	•
PDG	488867	4177329	1214	•		•	•	
PER1	511617	4183058	871			•	•	
PER2	511357	4183505	890			•	•	
PER3	511779	4183595	830			•	•	
PER4	511894	4183775	818			•	•	
PER5	511632	4183833	826			•	•	
PER6	511529	4183719	858			•	•	
PISA	509666	4168643	502		•	•	•	•
PLU	499117	4179835	2971	•		•	•	
ROC	500461	4200342	960	•		•	•	
SANT	515919	4178538	140			•	•	
SCOR	513799	4180818	526			•	•	
SGBO	513674	4167958	286		•	•	•	•
SGMB	514240	4176821	351			•	•	•
SSBI	519327	4183763	119			•	•	
STAZ	517466	4167441	47		•	•	•	•
STP	505487	4172033	1329	•		•	•	
SVEN	511353	4170771	436		•	•	•	•
TARC	519071	4174522	45		•	•	•	•
TDF	500087	4176707	2966	•		•		
TERR	513733	4185997	533			•	•	
TUR	490508	4174002	1326	•		•	•	
TVOL	507363	4171611	1048		•	•		

[a]See also Figure 1.

antenna models used during each survey. Precise ephemerides produced by the IGS are also used to achieve higher accuracy during the baseline computations [*Beutler et al.*, 1990].

[15] The data are processed using both GPS frequencies L1 and L2. In particular, their combination L3, called Iono free observable, is used for baselines longer than 10 km to eliminate the ionospheric effects. The use of the L3 observable always introduces a noise that becomes stronger than the ionospheric effect for short distances, so only the L1 frequency was used to process baselines shorter than 10 km, as is usually done for the Mount Etna network [see *Puglisi et al.*, 2004, and references therein].

[16] Data from NOT1, MATE and CAGL IGS stations (a map of IGS network for European region is available at http://igscb.jpl.nasa.gov/network/maps/all_eur.html) are introduced into the processing of the Etna 2001-A and Etna 2001-B surveys, in order to reference the Mount Etna network to the ITRF international frame. We cannot introduce IGS stations in the processing of other surveys because the relevant sessions were not long enough to guarantee the ambiguity fixing in the computations of baselines between Mount Etna and IGS stations. The data collected from the Permanent GPS network of the volcano (Figure 1) [*Bonaccorso et al.*, 2004] are introduced only into the processing of Etna 2001-A, Etna 2001-B, and Ionica 2001-B surveys.

[17] All the baseline solutions with fixed phase ambiguities, resulting from each survey processing, are then adjusted. Each adjustment is performed in two steps. First, the whole set of baseline solutions is adjusted according to the hypothesis of the inner constraints (in practice the network is fixed to its centroid); this step allows data consistency to be validated. Then the network is fixed assuming an appropriate set of coordinates for the reference frame.

[18] The Etna 2001-A and Etna 2001-B surveys is both adjusted by fixing the coordinates of the NOT1, MATE and CAGL IGS stations to the ITRF2000 [*Altamimi et al.*, 2002], calculated for the epoch 2001.6, to have a common reference frame (Table 2). Reference station coordinates are derived from the ITRF2000 solution, using the velocity model produced for each station by the IGS. We chose these surveys as reference for this study because they were carried out on the complete network, with longer measurement sessions (6 h on the external subnetwork and 24 h sessions on some permanent stations).

[19] In order to refer all networks considered in this study to a unique reference frame we keep fixed the coordinates of the IIV, CES, ROC, and CAS benchmarks (i.e., the external reference frame of Mount Etna [*Puglisi et al.*, 2004]) (Figure 1) computed with respect to the ITRF2000, epoch 2001.6, throughout the adjustments of all surveys considered in this work. A summary of the baseline processing for each survey is reported in Table 2. The results of the adjustments of each GPS survey are the station coordinates for each campaign.

[20] The coordinates of each GPS survey are compared to the others in order to estimate the displacement vectors and height variations of each station. The GPS stations height variations are spatially interpolated for each survey, gridding the values using the kriging method and taking into account the error variance, so as to obtain maps of the height variations above the investigated area (Figures 3a, 4a, 5a, and 5b). The 2-sigma formal error for the static measurements is typically 3–4 mm for the horizontal component, and about twice for the vertical component. For the stations belonging to the N-S profile, which are surveyed in

Table 2. Summary of the GPS Surveys and Processing

	Etna 2000	Ionica 2001-A	Etna 2001-A	Etna 2001-B	Ionica 2001-B
Time from	19 Jul 2000	16 Jan 2001	28 Jun 2001	23 Aug 2001	29 Oct 2001
Time to	28 Jul 2000	19 Jan 2001	11 Jul 2001	7 Sep 2002	30 Oct 2001
Number of stations	44	19	80	90	33
Number of measured baselines	368	190	3441	3862	616
Ephemeredes	precise	precise	precise	precise	precise
Searched solutions if distance >10 km	L3 fixed	L3 fixed	L3 fixed	L3 fixed	L3 fixed
Searched solutions if distance <10 km	L1 fixed	L1 fixed	L1 fixed	L1 fixed	L1 fixed
Bad solutions	7	14	72	53	1
Kind of adjustment	fully constrained	fully constrained	fully constrained	fully constrained	fully constrained
Fixed stations	IIV - CES - ROC	IIV - CAS	NOTO - MATE - CAGL	NOTO - MATE - CAGL	IIV - CAS
References system	ITRF 2000	ITRF 2000	ITRF 2000	ITRF 2000	ITRF 2000

semikinematic mode, the calculated uncertainty is about twice the static one [*Puglisi et al.*, 2004]. The values of the displacement vectors, for each comparison analyzed in this paper, are reported in the auxiliary materials.[1]

4. SAR Images Selection and DInSAR Processing

[21] The radar images processed and analyzed in this study were taken over Mount Etna by the ERS-2 satellite (Table 3). The choice of the pairs is based on two criteria. First, pairs having the smallest perpendicular baseline component are selected (to minimize geometrical decorrelation). Second, among them, we choose orbit pairs with different time windows and epochs in order to capture preevent, coevent, and postevent movements as well as short- and long-term deformations. The data set comprises both ascending (frame 747; at 2116 UT) and descending (frame 2853; at 0940 UT) orbit data. Figure 2 shows the time coverage of GPS and DInSAR data.

[22] The raw data are processed to zero compensated Doppler, slant range projection, phase-preserved single look complex (CEOS-SLC) images. The procedure used for the generation of interferometric products relevant to the selected image pairs is the so-called "two pass interferometry" [*Massonnet and Feigl*, 1998]. This method requires two SAR images to generate an interferogram that is correlated with topography and changes in topography. To analyze the surface displacements, the topography-dependent part of the interferogram is eliminated. This is done by using an independent DEM and converting the height values into synthetic phase values. In a next step, the phase values of the real and synthetic interferogram have to be subtracted from each other. This approach removes topographic fringes, leaving only those related to ground motion, atmospheric path delay and/or errors in the DEM. A photogrammetric DEM, with a measured vertical accuracy in the order of 10 m is used as a source for the topographic information. To coregister the two images and calculate the interferometric geometry, we use the precise orbits of the ERS2 satellite, produced at the Delft Institute for Earth Oriented Space Research (DEOS).

[23] Since the phase difference of the image pair corresponds to the change in the round-trip path length of radar waves to ground targets, an interferogram is similar to a contour map of the change in distance to the ground surface along the Line of the Sight (LOS) of the satellite. Each contour line, or fringe, represents 28 mm, i.e., half the wavelength of the ERS radar.

[24] At the beginning of 2001, the ERS-2 gyroscopes had serious mechanical problems and could not be used to get the necessary platform attitude information. As a consequence, the Doppler Centroid of the ERS-2 images varied widely and randomly from one observation to the next, often making the generation of SAR interferograms impossible. A back-up attitude control system was activated and tuned by the ESA-ESRIN staff, and in June 2001, the interferometric capability of ERS-2 was partially recovered. In fact, the POLIMI team, in cooperation with TRE (POLIMI commercial spin-off), was able to obtain clear surface deformation maps related to the 6 June, 11 July, and 15 August 2001 passes.

5. Ground Deformation Patterns and Models

[25] In sections 5.1–5.4 we analyze in detail the ground deformation patterns affecting the volcano edifice before, during and after the eruption by exploiting all the available GPS and DInSAR data. In general, we use GPS data (by weighting horizontal and vertical displacements with the respective experimental errors) to perform a first attempt at fixing the parameters of the ground deformation sources and the DInSAR data to refine it; differences eventually obtained between the two surveying techniques will be discussed later, because they are important for understanding local anomalies. Taking advantage of the fact that the Etna 2001-A and Etna 2001-B surveys have the most complete geometrical configuration on the eastern flank of the volcano, we anticipate that the comparison between

Table 3. Raw ERS SAR Available Data

Satellite	Orbit	Track	Frame	Date	Time (UT)
ERS-2	28039	129	747	30 Aug 2000	2116
ERS-2	28633	222	2853	11 Oct 2000	0941
ERS-2	29134	222	2853	15 Nov 2000	0941
ERS-2	29542	129	747	13 Dec 2000	2116
ERS-2	32047	129	747	6 Jun 2001	2116
ERS-2	32548	129	747	11 Jul 2001	2116
ERS-2	33049	129	747	15 Aug 2001	2116
ERS-2	34144	222	2853	31 Oct 2001	0941

[1] Auxiliary materials are available in the HTML. doi:10.1029/2006JB004811.

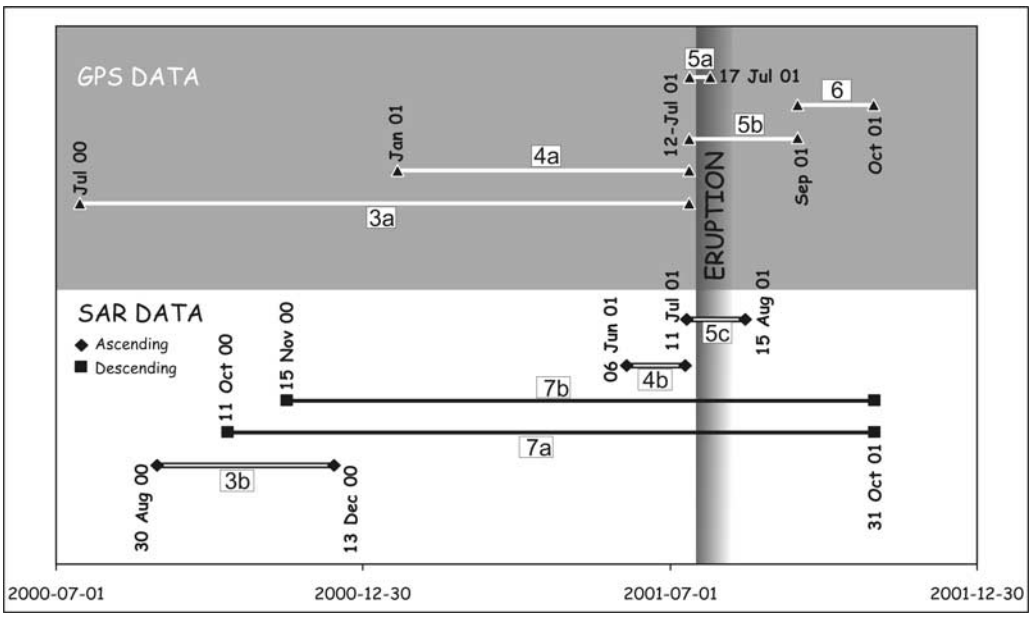

Figure 2. Time coverage of GPS and DInSAR data. The various data sets are labeled with the number of the figure in which the data are presented.

these two surveys will be used to recalculate all the parameters of the subhorizontal dislocation plane beneath the eastern flank, already deduced from previous GPS data [*Bonforte and Puglisi*, 2003] and frequently used in modeling ground deformation of eastern flank, even during recent eruptions [e.g., *Puglisi and Bonforte*, 2004; *Bonaccorso et al.*, 2006]. The position and the geometry of the plan obtained in such a way are keep fixed for modeling the other comparisons, with ground deformation data available for only part of the network. It seems reasonable, indeed, that this plan, which is adopted to model one of the longest-lasting and continuous movement of Mount Etna, will maintain its geometry throughout the 2-year interval analyzed in this paper. Furthermore, this choice will reduce the parameters to be inverted, allowing studying a period for which there are relatively few suitable data (e.g., January–July 2001).

5.1. Ground Deformation Before the Eruption

[26] Four ground deformation data sets are available to investigate the year before the eruption: two obtained by comparing GPS campaigns and two from DInSAR analysis. By appropriately combining these data sets we can investigate different time intervals. The 1-year preceding the eruption is studied by comparing the Etna 2000 and Etna 2001-A surveys. The other three data sets, which cover shorter time intervals, allow either to tune the parameters of deformation sources inferred by analyzing the 1-year interval or to integrate the structural setting by analyzing local data. In particular, the available ground deformation data set allows examining this 1-year time period in detail, by investigating the August–December 2000, the January–July 2001 and the June–July 2001 intervals by using DInSAR movements maps of the entire volcano for the first and third periods and GPS data of the southern-east flank for the second one (Figure 2).

5.1.1. Deformation Sources From July 2000 to July 2001

[27] During this period, we observe a general radial pattern of surface displacements on the volcano, with uplift in the order of 6 cm centered on its upper northwestern flank (Figure 3a). This deformation is inverted using a *Mogi* [1958] pressure source model and a Simplex optimization technique [*Nunnari et al.*, 1995], which searches the minima of a response function in the whole space of parameters, without any a priori constraints. Since the parameters P (change of the hydrostatic pressure in the sphere) and a (radius of the spherical source) cannot be solved independently in the *Mogi* [1958] model, to simplify the minimum search the product Pa^3 is assumed as strength of the source (S), according to *McTigue* [1987]. The parameter space is sampled by running about 90 minimum function searches, each search starting from a different set of parameter values. Analogously with similar inversions performed in previous studies [e.g., *Puglisi and Bonforte*, 2004], starting points are arranged on a 10 km spaced grid; for each horizontal position, two different depths (3 and 5 km) are assumed and, for each depth, 2 different strength values are tested (3×10^{18} and 5×10^{18} Pa m^3). Also a start point located beneath the summit craters area is used, for which values of 1, 3 and 5 km for the depth and 1, 2, 3, 4 and 5×10^{18} for the strength are assumed; all the parameter searches converge to a deformation source beneath the upper western flank of the volcano at a depth of about 6.2 km bsl. In order to better fit the deformation observed on the eastern and southern flanks, the two subhorizontal dislocation planes beneath the southern and eastern flanks [*Bonforte and Puglisi*, 2003], were added to the inversions adopting procedures used in previous studies [e.g., *Puglisi and Bonforte*, 2004]. As anticipated, the position and the geometry of the eastern subhorizontal plane are thus kept fixed to values obtained by inverting the July–September 2001 comparison (see section 5.1.2).

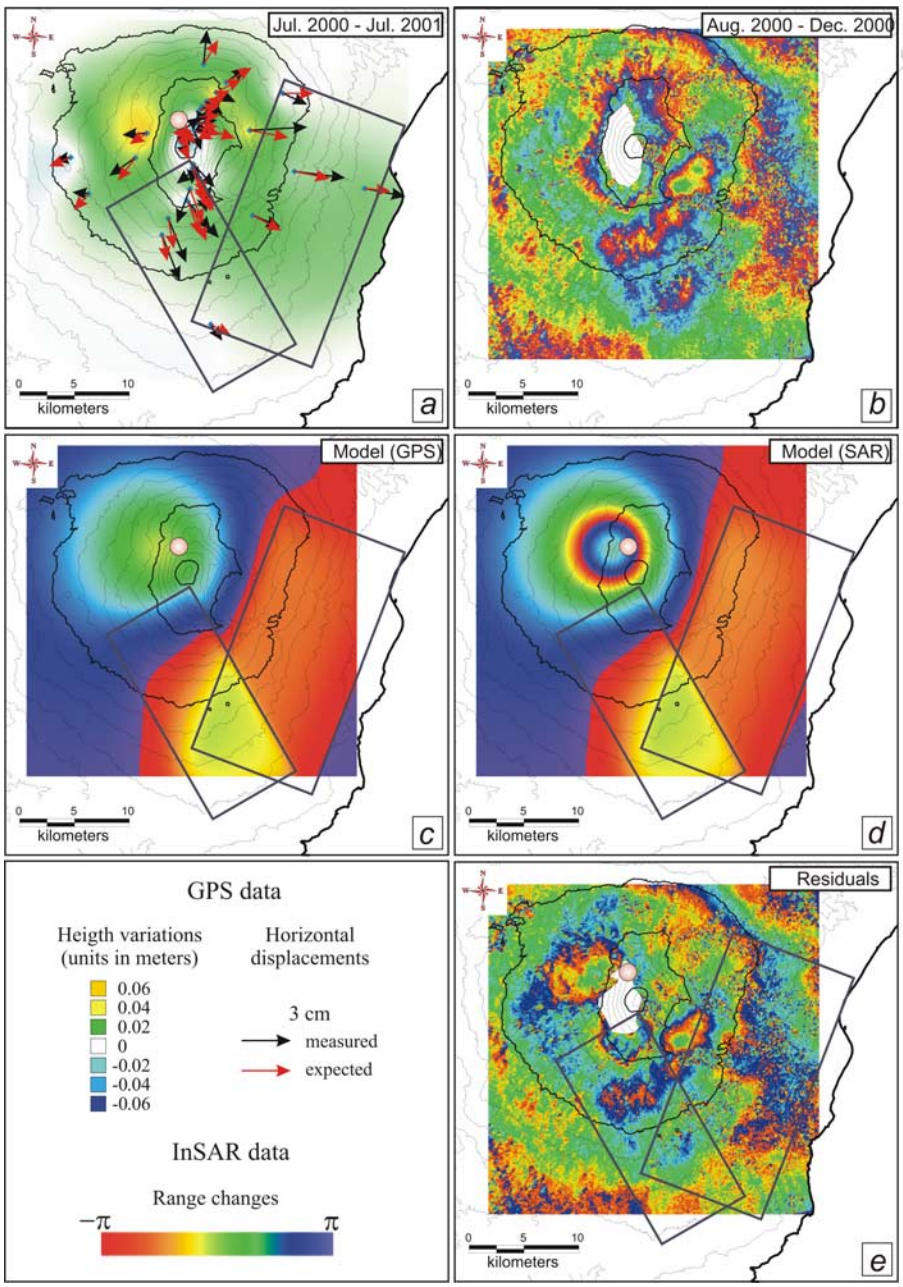

Figure 3. (a) Displacements measured by GPS from July 2000 to July 2001 and corresponding inferred model (parameters in Table 4); (b) DInSAR data relevant to the August–December 2000 ERS-2 ascending pair (negative values within the Valle del Bove area are produced by the 1991–1993 lava flows compaction); (c) synthetic interferogram calculated from sources inferred by GPS inversion; (d) synthetic interferogram obtained by combining GPS and DInSAR final model; (e) residuals between DInSAR data and the synthetic interferogram. Circles represent pressure sources, while boxes represent the surface projections of planar sources.

As concerns the southern subhorizontal plane, we fix its geometry to the values found by *Bonforte and Puglisi* [2003] because the geometry of the considered network does not allow to better constrain the position and the geometry of this structure. Thus, here we searched only the motion of the two subhorizontals planes in the 2000–2001 period. The final results of the inversion are summarized in Table 4 and Figures 3a and 8a.

5.1.2. Deformation Sources From August to December 2000

[28] The interferogram (Figure 3b) of the August and December 2000 ERS-2 ascending passes, shows an apparent uplift (1 fringe) affecting the upper part of the volcano. This interferometric feature could be produced either by tropospheric effects or by actual ground deformation. In order to solve this ambiguity, we check the consistency of this interferogram with that expected by applying the model

Table 4. Parameters of the Sources Modeled for the July 2000 to July 2001 Comparison[a]

Parameters	Pressure Source (PS1)	Southern Subhorizontal Plane (SSP)	Eastern Subhorizontal Plane (ESP)
Longitude (km)	498.18 ± 0.3	504.69	504.20
Latitude (km)	4180.75 ± 0.3	4168.59	4172.03
Azimuth (deg.)		N150°E	N21°E
Depth (km)	6.2 bsl ± 0.5 4.2 bsl[b]	0.5 asl	1.4 bsl
Length (km)		20	26.4
Width (km)		8.7	12.34
Dip (degrees)		18°W	11.6°E
Strike (cm)		0.5 left-lat. ± 0.02	0.8 left-lat ± 0.05
Dip (cm)		0.5 normal ± 0.03	2.8 normal ± 0.05
Opening (cm)		−1 ± 0.02	−0.1 ± 0.02
S (10^{17} Pa m^3)	1.3 ± 0.3		

[a]The modeling of the dislocations refers to the half-space. Easting, northing, and depth refer to the center of the top of the dislocation. Strike slip is positive if left lateral, and dip slip is positive if normal. S is the strength of the Mogi source, according to *McTigue*'s [1987] assumption.
[b]This is the source PSIA, from DInSAR data.

assessed above by using GPS vector displacements (Table 4). Because of the shorter time interval covered by the interferogram (4 months versus 1 year for the GPS surveys), the strength of the pressure source and the dislocations along the sliding planes are reduced to 1/3. A first synthetic interferogram resulting from the combination of the sources modeled from GPS data is very similar to that reported in Figure 3b, although it produces a weaker deformation but affecting a wider area with respect to the measured one (Figure 3c). This suggests that atmospheric artifacts are negligible at the scale of the volcano and probably limited in small areas in the interferogram (e.g., on the lower eastern flank, along the coast, or in the "bubbles" on the middle southern flank). Thus, in order to improve the fitting of the observed fringe pattern, we perform a trial and error search, which shifted the center of the pressure source 2 km shallower (Figure 3d). The residuals (Figure 3e) show that the misfit between the measured and synthetic interferograms is within ±0.5 interferometric fringes, which is an acceptable value for a single interferogram [*Beauducel et al.*, 2000]. The model fits the GPS data satisfactorily (average misfit of 0.8 cm and 2.6 cm for the horizontal and vertical displacements, respectively). The parameters of the final model obtained combining GPS and DInSAR data are reported in Table 4 and Figure 8a.

5.1.3. Deformation Sources From January to July 2001

[29] The GPS data available for this 6-month period allow only studying the lower eastern flank dynamic, because here we used the Ionica 2001-A survey data set. The comparison between the Ionica 2001-A and Etna 2001-A surveys shows a marked uplift of the westernmost station (at about 1000 m of altitude), suggesting that the uplift of the upper part detected by DInSAR between August and December 2000 extended downslope (Figure 4a). Furthermore, GPS data also show subsidence on a narrow NNW-SSE trending area. These observations can be explained assuming the activation of two NNW-SSE dislocation planes, roughly coincident with the TFS and San Leonardello fault (SLF), and the eastern subhorizontal plane. The values of the strike, depth, width and dip of the dislocations are chosen from the literature [*Lanzafame and Bousquet*, 1997; *Gresta et al.*, 1990], thus only their position, length and movements are inverted. Since there are not enough data to invert the parameters of the eastern subhorizontal plane (see the previous paragraph), we fix the position and the geometry of this structure to that obtained by studying the Etna2001-A−Etna2001-B comparison, and we invert only the parameters of the movement. The results of this inversion are reported in Table 5 and Figure 4a (the misfits with horizontal and vertical displacements are 0.6 and 1.2 cm, respectively).

5.1.4. Deformation Sources From June to July 2001

[30] Finally, the interferogram of the 6 June to 11 July 2001 period (Figure 4b) suggests that during the month before the eruption onset no significant deformations occurred except a general small inflation, in agreement with the sources already inferred from GPS data (see Table 4 and Figures 3 and 8a).

5.2. Ground Deformations During the Eruption

[31] Here we consider the ground deformations measured by comparing the Etna 2001-A and Etna 2001-B surveys as well as the measurements carried out on 17 July on significant parts of the north-south and east-west profiles. The analysis is completed by taking into account the 11 July to 15 August 2001 interferogram. Furthermore, the results obtained in a previous paper [*Bonforte et al.*, 2004] are considered to improve the analysis of the deformations during the eruption.

5.2.1. Deformation Sources During the Dike Intrusion, Before the Vents Opening

[32] In this paper, a set of GPS data collected during the days of the rising of the intrusion, never analyzed before, is exploited. The deformations obtained comparing the static survey carried out on 17 June with the measurements of 11 June on selected benchmarks of the upper flanks of the volcano are reported in Figure 5a. The deformation pattern is evidently related to the N-S intrusion that was rising during these days. Further evidence is the effect of the propagation from north to south of the fracture fields forming on 17 July [*Acocella and Neri*, 2003] that produces the southward vectors of the benchmarks located close to the southern end of the UV, at about 2500 m asl. To transform this qualitative analysis into an analytic inversion

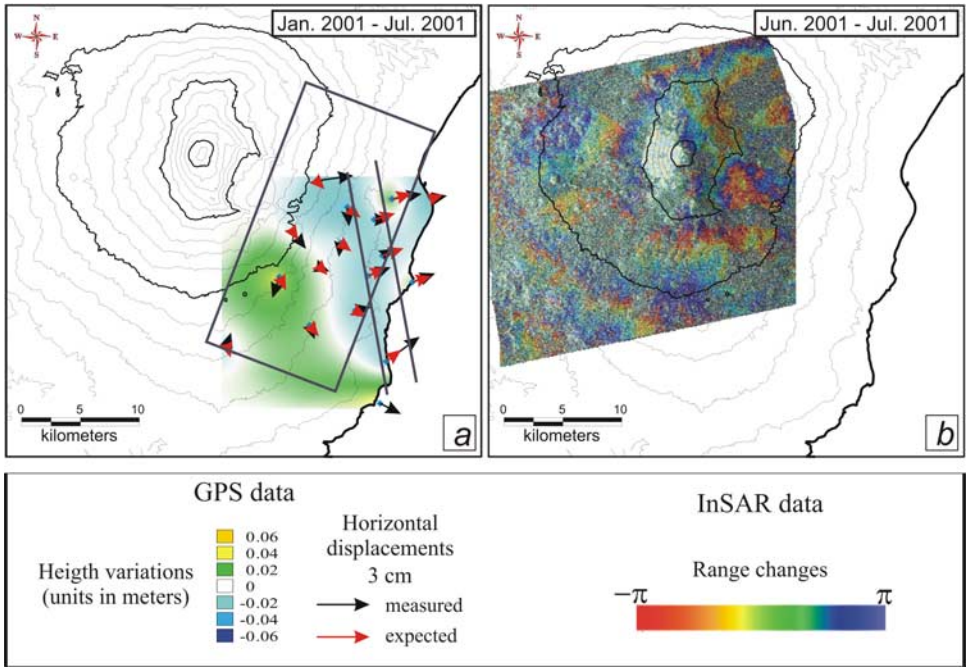

Figure 4. (a) GPS displacements from January to July 2001 and corresponding inferred model (parameters in Table 5); (b) DInSAR data relevant to the June 2001 to July 2001 ERS-2 ascending pair. The lines and boxes represent the surface projections of planar sources.

is quite difficult, because during the 17 June survey the fracture fields were forming so the ideal conditions of "static deformations" are not guaranteed. Despite these difficulties, a simple analytic inversion is attempted by starting from the dike's parameters obtained by *Bonaccorso et al.* [2002], to attempt inferring the final phases of the magma rising. The results are reported in Table 6 and Figures 5a and 8b, showing a shallower and more westernward dike than the one used to start the inversion, with a slightly bigger volume than obtained by *Bonaccorso et al.* [2002].

5.2.2. Deformation Sources During the Vents Opening and Lava Flows Outpouring

[33] The GPS survey carried out on the whole network in September 2001, compared to that carried out in July 2001, confirmed the strong deformation of the edifice (Figure 5b), showing displacement vectors of several tens of centimeters on the upper part, and a N-S contraction revealed by the convergence of the southern and northern benchmarks of the network. Also evident is a significant subsidence centered south of the summit area, which is characterized by the formation of grabens around the eruptive fractures [*Acocella and Neri*, 2003]. The intensity of the deformation progressively decreases downslope, becoming negligible along the coastline. This deformation pattern is also confirmed by the ascending interferogram of the 11 July to 15 August 2001 pair of SAR images, which shows two different areas with opposite LOS deformation of the volcano (Figure 5c). In particular, the area, located in the Valle del Bove moves away from the sensor, while the area located on the western flank of the volcano approaches the sensor.

Table 5. Parameters of the Sources Modeled for the January 2001 to July 2001 Comparison[a]

Parameters	Eastern Subhorizontal Plane (ESP)	Timpe Fault System (TFS)	San Leonardello Fault (SLF)
Longitude (km)	504.20	513.63 ± 0.8	516.08 ± 0.5
Latitude (km)	4172.03	4167.33 ± 0.2	4168.35 ± 0.1
Azimuth (deg)	N21°E	N12°W	N12°W
Depth (km)	1.4 bsl	0.3 asl	0.3 asl
Length (km)	26.4	19 ± 0.9	19 ± 0.9
Width (km)	12.34	5.5 (4.5)	5.5 (4.5)
Dip (deg)	11.6°E	89°E	89°E
Strike (cm)	0.4 right-lateral ± 0.04	0.9 left-lateral ± 0.06	0 ± 0.07
Dip (cm)	0.2 normal ± 0.06	0.4 (east up) ± 0.08	3.1 (east up) ± 0.09
Opening (cm)	0 ± 0.03	0.3 ± 0.04	0 ± 0.05

[a]The modeling of the dislocations refers to the half-space. Easting, northing, and depth refer to the center of the top of the dislocation. Assuming an average altitude of the GPS network of 1000 m asl, the widths reported for the Timpe fault system (TFS) and San Leonardello fault (SLF) are relative to it. Considering that the topography is below the reference level in the easternmost part of the volcano, the "true" width below the ground could be estimated as the values reported in brackets and the depths are 0 (i.e., it coincides with the ground altitude at the fault trace). Strike slip is positive if left lateral, and dip slip is positive if normal.

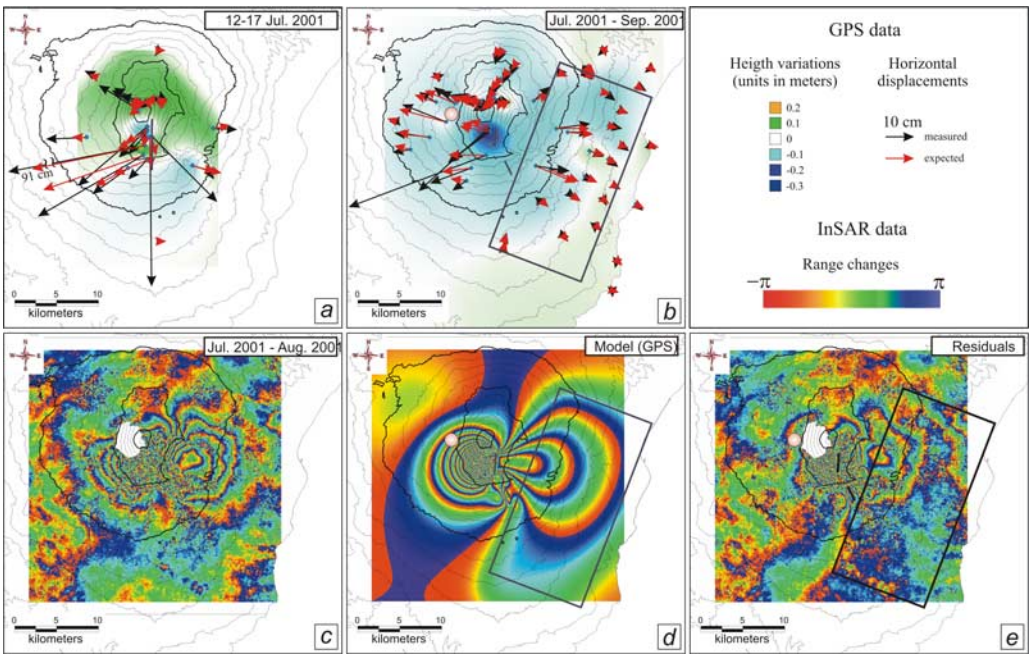

Figure 5. (a) GPS displacements from 12 to 17 July and corresponding model (parameters in Table 6); (b) GPS displacements from July to September 2001 and corresponding model (parameters in Table 7); (c) DInSAR data relevant to the July–August 2001 ERS-2 ascending pair; (d) calculated synthetic interferogram; (e) residuals between DInSAR data and the synthetic interferogram. Circles represent pressure sources, while lines and boxes represent the surface projections of planar sources.

[34] This deformation pattern is consistent with a N-S trending intrusion cutting the volcano edifice. The July–September 2001 GPS vectors are modeled by starting our search from three deformation sources (Figure 5b), which were active in summer 2001, as testified or suggested by independent studies previously performed. The three sources are (1) the eruptive dike modeled by *Bonaccorso et al.* [2002], (2) the NNW-SSE fault modeled by *Bonforte et al.* [2004], and (3) the subhorizontal plane used to model the eastward movement of the eastern flank during the 1994–1998 time interval [*Bonforte and Puglisi*, 2003; *Puglisi and Bonforte*, 2004]. This search does not consider the southern subhorizontal plane previously used for inverting the 2000–2001 comparison since the eruption destroyed some benchmarks on the southern half of the N-S kinematic profile, deteriorating the network geometry and preventing fixing the parameters of this structure. This is obviously a limitation of our modeling, but we prefer to avoid imposing an arbitrary movement of this source (its geometry and location could, indeed, be assumed from previous results), not to run the risk of an uncontrolled perturbation of our model, leading to a misinterpretation of the volcano dynamics. Conversely, thanks to the denser network on the eastern side of the volcano in 2001 with respect to 1994, when this structure was studied for the first time [*Bonforte and Puglisi*, 2003], it was possible to recalculate all parameters of the eastern sliding plane. Finally, we kept fixed the parameters of the NNW-SSE fault to those found by *Bonforte et al.* [2004] using a much denser network in this area with respect to that considered in July–September 2001 comparison. Regarding the dike and the subhorizontal eastern plane, we performed our inversion by using a least squares approach and starting from the published parameters by *Bonaccorso et al.* [2002] and *Puglisi and Bonforte* [2004], respectively.

[35] The main results of the inversion are relevant for to the location and dimension of the dike and the geometry of the subhorizontal plane (Figures 5b and 8b). The resulting dike has a few differences with respect to that published by *Bonaccorso et al.* [2002] and used here as starting point: it is slightly farther southwest (about 0.7 km) and is wider (about 1.2 km), resulting in a larger volume (about 1.2 times), even though it shows a lesser opening. The

Table 6. Parameters of the Sources Modeled for the 12 to 17 July 2001 Comparison[a]

Parameters	Dike (D)
Longitude (km)	500.65
Latitude (km)	4174.66 ± 0.005
Azimuth (deg)	N0°E
Depth (km)	1.6 asl
Length (km)	3.14 ± 0.006
Width (km)	0.77 ± 0.003
Dip (deg)	89°E
Strike (cm)	96.87 ± 0.271
Dip (cm)	−82.17 ± 0.210
Opening (cm)	367.19 ± 0.411

[a]The modeling of the dislocations refers to the half-space. Easting, northing, and depth refer to the center of the top of the dislocation. Strike slip is positive if left lateral, and dip slip is positive if normal.

Table 7. Parameters of the Sources Modeled for the July 2001 to September 2001 Comparison[a]

Parameters	Dike (D1)	Pressure Source (PS2)	Eastern Fault (EF)	Eastern Subhorizontal Plane (ESP)
Longitude (km)	500.65 ± 0.04	495.42	502.20	504.20 ± 0.06
Latitude (km)	4175.50 ± 0.04	4178.23	4171.80	4172.03 ± 0.13
Azimuth (deg)	N3.4°E ± 0.7fs		N26°W	N21°E ± 0.2
Depth (km)	1.6 asl ± 0.01	9 bsl	1.04 asl	1.4 bsl ± 0.03
Length (km)	2.34 ± 0.05		1.9	26.4 ± 0.1
Width (km)	3.55 ± 0.02		2.5	12.34 ± 0.1
Dip (deg)	89°E ± 0.1		73°E	11.6°E ± 0.3
Strike (cm)	0		40 right-lat.	0.8 left-lat. ± 0.04
Dip (cm)	0		13 normal	2.6 normal ± 0.05
Opening (cm)	251.7 ± 0.2		18	−1.6 ± 0.04
S (10^{17} Pa m^3)		−3.2		

[a]The eastern fault is fixed to the solution found by *Bonforte et al.* [2004]. The modeling of the dislocations refers to the half-space. Easting, northing and depth refer to the center of the top of the dislocation. Strike slip is positive if left lateral, and dip slip is positive if normal. S is the strength of the Mogi source, according to *McTigue*'s [1987] assumption.

main changes in the subhorizontal plane are the width, which is now 12 km instead of 9 km, and the dip angle that is reduced to 12° instead of 19°. The higher number of stations, in fact, allows the sliding plane to be better defined at low altitude.

[36] By analyzing the residuals obtained after subtracting the deformation expected from this model and the observed one at the GPS stations, we can investigate the effect produced by other sources eventually active during the eruptions and, specifically, the Mogi-type source inferred during the year preceding the volcanic event. Thus the residuals are inverted using the Simplex method above described, by running more than 200 tests. All of them converge rapidly to a depressurization source located at about 9 km bsl, centered about 3 km southwestward with respect to that inferred before the eruption (Table 7 and Figure 8b).

[37] The ground deformation pattern calculated from this source setting, produces GPS displacement vectors in good agreement with that observed (Figure 5b). Because of the very large deformations measured in this case, the average misfits on the horizontal and vertical displacements (now 3.7 and 5.9 cm, respectively) are larger than obtained for the preeruptive period. The synthetic interferogram for the July–August pair (Figure 5d) also concurs with the experimental data (Figures 5c and 5e), producing residuals within ±1 interferometric fringe on almost all the volcano, except small areas falling in the near field of the intrusion (i.e., where the deformations are far from elastic). Because the interferogram did not reach the coastline, due to satellite attitude control problems, it is not possible to check its agreement with the model proposed by GPS data in the lower eastern flank of the volcano.

5.3. Ground Deformation After the Eruption

[38] The displacements resulting by comparing the Etna 2001-B and the Ionica 2001-B surveys (Figure 6) show a maximum on the lowest flank that gradually decreases toward the upper part.

[39] To invert these data, we adopt similar procedures and assumptions on the structural framework as for the January–July 2001 comparison (Table 8). The misfits with the horizontal (0.7 cm) and vertical (0.6 cm) displacements are similar to those obtained for the preeruptive models. The SLF shows again a significant uplift of its eastern side (Table 8), and the TFS shows a significant dextral dislocation, in good agreement with the focal solution (Figure 6) [*Azzaro et al.*, 2002]; the eastern subhorizontal plane has a sliding (10 cm/a), which is in the same order as that calculated for the eruptive period (17 cm/a) (Table 8), although a bit slower. Unfortunately, no interferometric data are available for this time coverage, so it is not possible to

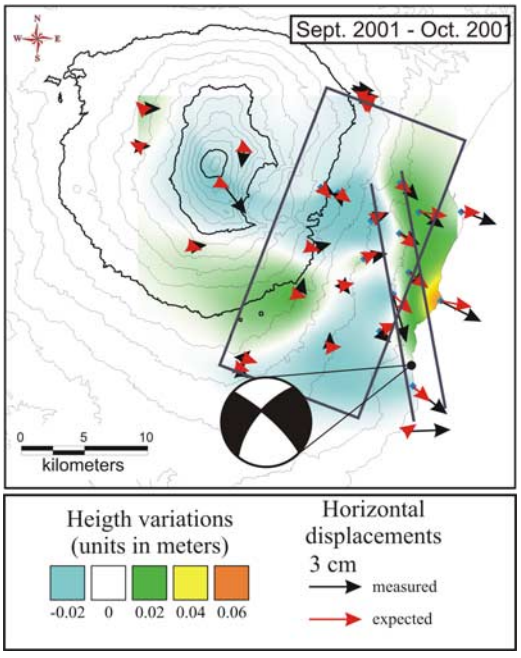

Figure 6. GPS displacements from September to October 2001 and corresponding calculated model (parameters in Table 8). Location and focal solution of the main shock of the seismic swarm occurring in October on the lower southeastern flank of the volcano are also reported. Lines and boxes represent the surface projections of planar sources.

Table 8. Parameters of the Sources Modeled for the September 2001 to October 2001 Comparison[a]

Parameters	Eastern Subhorizontal Plane (ESP)	Timpe Fault System (TFS)	San Leonardello Fault (SLF)
Longitude (km)	504.20	513.63 ± 0.8	516.08 ± 0.5
Latitude (km)	4172.03	4167.33 ± 0.2	4168.35 ± 0.1
Azimuth (deg)	N21°E	N12°W	N12°W
Depth (km)	1.4 bsl	0.3 asl	0.3 asl
Length (km)	26.4	19 ± 0.9	19 ± 0.9
Width (km)	12.34	4.5	4.5
Dip (deg)	11.6°E	89°E	89°E
Strike (cm)	0.6 right-lateral ± 0.04	1.9 right-lateral ± 0.05	0.1 right-lateral ± 0.06
Dip (cm)	1.5 normal ± 0.05	1.1 (east up) ± 0.07	2.9 (east up) ± 0.08
Opening (cm)	0.3 ± 0.03	−0.4 ± 0.04	0.8 ± 0.05

[a]For the width and depth parameters related to the Timpe fault system (TFS) and San Leonardello fault (SLF) refer to Table 5 caption. The modeling of the dislocations refers to the half-space. Easting, northing, and depth refer to the center of the top of the dislocation. Strike slip is positive if left lateral, and dip slip is positive if normal.

study local effects possibly arising from the activation of the faults cutting this area.

5.4. Long-Period Interferograms

[40] The October 2000 to October 2001 (Figure 7a) and November 2000 to October 2001 (Figure 7b) descending pair interferograms encompass the whole eruptive period. Both interferograms show the volcano's western flank moved about 20 cm away from the sensor (that is looking from the eastern side), while there is too much noise on the eastern flank, especially in the October 2000 to October 2001 pair, to measure the ground deformation pattern in this area. Because of the long time span of these interferograms, extending from the preeruptive to the posteruptive period, they should show the effects of the different ground deformation sources, active at different times, modeled by the previous short-period analyses. A trial-error approach is used to refine the model parameters for this inversion. The sliding for the eastern subhorizontal dislocation is calculated, for each component of motion, by cumulating the values related to each time interval previously considered. The first trials show that the westward displacement caused on the western flank by the intrusion of the eruptive dike was not strong enough to produce so many fringes as observed. Thus, we assume that the same source that inflated before the eruption (see Table 4), depressurized during and after the eruption. In this way, we succeed in fitting the observed synthetic interferogram by refining the center of the pressure source alone, which is moved 1 km westward with respect to the solution found for the August 2000 to December 2000 pair. Even in that case the residuals remain within ±0.5 interferometric fringes over the volcano, with the only exception of the near field of the intrusion (Figure 7d). Results of the long-term modeling are reported in Table 9 and Figure 8c.

6. Discussion

[41] The ground deformation data (GPS and DInSAR) allow modeling volcanic and tectonic features active before, during and after the 2001 Mount Etna eruption. These models enable reconstructing the evolution of these features through the one and a half-year period encompassing the eruptions and to compare this reconstruction with the results of published studies.

6.1. Shallow Intrusions

[42] The dike triggering the eruption and feeding the southern eruptive fissure system inferred in this work agrees well with the trend and location of the LV fissure system. However, when comparing this result with previous published studies, based on ground deformations, this model lies somewhere between those obtained by *Bonaccorso et al.* [2002] and *Lundgren and Rosen* [2003], who inverted deformations measured by permanent GPS and tilt stations, and DInSAR maps, respectively. Not only does the volume of this dike (20.6×10^6 m^3) fall between those obtained from the previous studies (17.7×10^6 m^3 from *Bonaccorso et al.* [2002] and 23.2×10^6 m^3 from *Lundgren and Rosen* [2003]) but also the location has the same characteristics (e.g., the projection of the center of this model is about 300 m west of the *Bonaccorso et al.* [2002] dike's projection and about 2 km east of the projection of the dislocation set hypothesized by *Lundgren and Rosen* [2003]). The discrepancies among these models could be due to the differences either in the time interval and/or in the data set and/or the modeling scheme, as resulting from the following considerations.

[43] *Bonaccorso et al.* [2002] modeled ground deformations for the 12 July to 15 July period, i.e., their data set stops 2 d before the vents opened. This data set constrained a dike located slightly eastward with respect to the actual fissure system, with its top about 2 km below the volcano surface. Our study, conversely, encompasses the opening of the vents, by modeling the data relevant to July–September 2001, and considers data from more stations, some of which are close to the eruptive fissures. These considerations suggest that the discrepancy is only apparent, because this study and the *Bonaccorso et al.* [2002] model depict the intrusion at different steps. Indirect proof of this conclusion came from the result of the inversion of 11–17 July vectors (Table 6) which infers a dike having parameters and volumes somewhere between those published by *Bonaccorso et al.* [2002] and those reported in Table 7. As confirmed by seismic data [*Falsaperla et al.*, 2005], the dike reached a relatively shallow depth already on 12–13 July; this was the intrusion modeled by *Bonaccorso et al.* [2002]. Afterward, the dike moved westward during its rising, appearing at the surface on the current fissure system; the models reported in Tables 6 and 7 thus refer to two successive steps of the dike

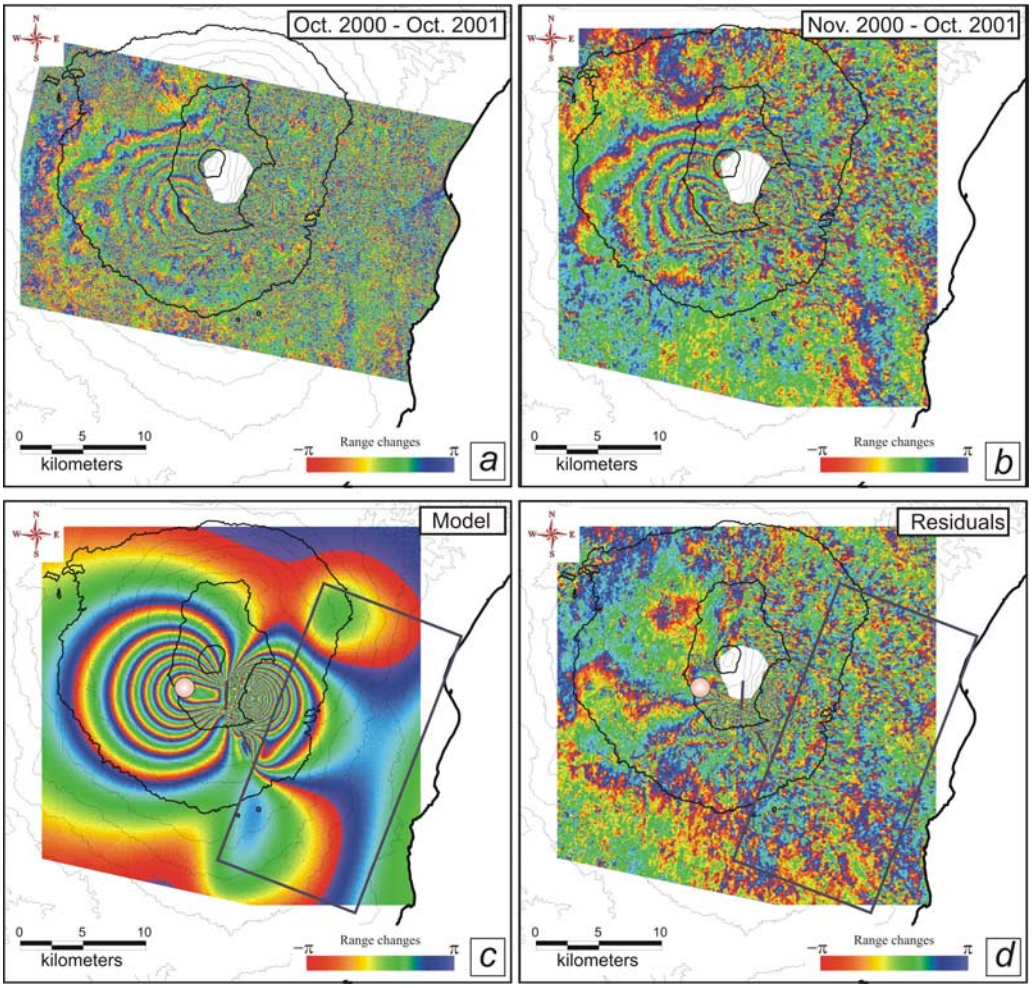

Figure 7. Ground deformation on Mount Etna and proposed models after the end of the 2001 lateral eruption. Circles represent pressure sources, while lines and boxes represent the surface projections of planar sources. DInSAR data relevant to the (a) October 2000 to October 2001 and (b) November 2000 to October 2001 ERS-2 descending pairs; (c) synthetic interferogram calculated by considering the sources reported in Table 9; (e) residuals between DInSAR data (Figure 7b) and the synthetic interferogram.

intrusion: just before it surfaced (in Table 6), and after the vent opening (in Table 7). It is noteworthy that the position of the dislocation reported in Table 6 corresponds to the low-Qp feature (<50 Qp) identified by *Martínez-Arévalo et al.* [2005], forming a sort of "bulge" between 0 and 1.5 km asl (Figure 8b and auxiliary materials). This suggests that from 15 to 17 July the intrusion "attempted" to propagate downward with respect to the lower end of the LV fissure system.

[44] By summarizing this temporal reconstruction of the intrusion and the geometry of the dike resulting from the different time intervals analyzed in this paper and by *Bonaccorso et al.* [2002], the dike actually seems to have a sigmoid type shape, because the shallow part is westward with respect to its deeper part (Figure 8b); this shape also agrees with the location of earthquake hypocenters [*Martínez-Arévalo et al.*, 2005]. This consideration indicates that the rising of the dike during the last kilometer was probably driven by the local stress field, which near the surface of the steep western flank of the Valle del Bove rotates its σ_1 parallel to the volcano surface (i.e., σ_3 is orthogonal to

Table 9. Parameters of the Sources Modeled for the October 2000 to October 2001 Comparison[a]

Parameters	Pressure Source (PS3)	Dike (D1)	Eastern Fault (EF)	Eastern Subhorizontal Plane (ESP)
Latitude (km)	497.18	500.65	502.20	504.20
Longitude (km)	4176.23	4175.50	4171.80	4172.03
Azimuth (deg)		N3°E	N26°W	N21°E
Depth (km)	4.2 bsl	1.6 asl	1.04 asl	1.4 bsl
Length (km)		2.34	1.9	26.4
Width (km)		3.55	2.5	12.34
Dip (deg)		89°E	73°E	11.6°E
Strike (cm)		0	40 right-lat.	1.0 right-lat
Dip (cm)		0	13 normal	6.9 normal
Opening (cm)		251.7	18	−1.4
S (10^{17} Pa m^3)	−1.8 ± 0.3			

[a]The modeling of the dislocations refers to the half-space. Easting, northing, and depth refer to the center of the top of the dislocation. Strike slip is positive if left lateral, and dip slip is positive if normal. S is the strength of the Mogi source, according to *McTigue*'s [1987] assumption.

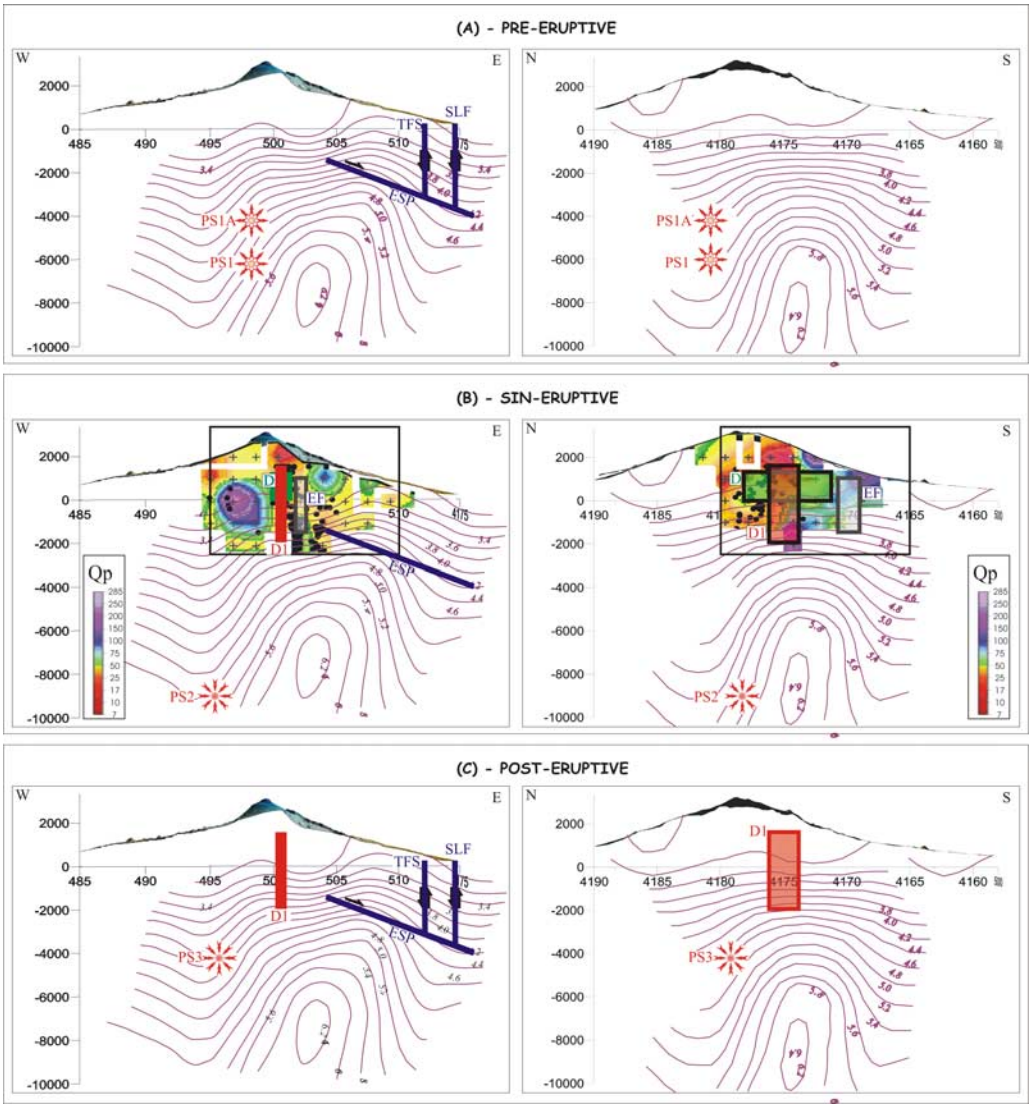

Figure 8. East-west and north-south cross sections showing the locations of the ground deformation sources modeled in this paper: (a) preeruptive models (sources from Tables 4 and 5); (b) syneruptive models (sources from Tables 6 and 7, superimposed to the Qp tomography obtained by *Martínez-Arévalo et al.* [2005]); (c) syneruptive and posteruptive models (sources from Tables 8 and 9). The isolines indicate the Vp values resulting from the *Chiarabba et al.* [2000] tomography. Numbers on the horizontal axes are UTM coordinates; thus the scale is in km. Vertical scale is in meters with respect to the sea level. The black points in Figures 8b indicate the positions of the earthquake hypocenters. A zoom of Figures 8b is provided as Figure S1.

the western wall of the Valle del Bove) as suggested by analog models performed by *McGuire* [1989] and confirmed by analytical models [e.g., *Dahm*, 2000].

[45] *Lundgren and Rosen* [2003] modeled the intrusion as a complex system of nine Okada-type sources, whose azimuth is rotated about 10° anticlockwise with respect to the LV fracture system. We suppose that the disagreement of their results with both geological evidences and our model depends on the peculiar modeling scheme adopted by Lundgren and Rosen. The azimuth they imposed corresponds to that of the upper part of the UV fissure system [*Acocella and Neri*, 2003] whose formation is due to a radial shallow intrusion from South-East crater, which is independent from the dike feeding the LV. Furthermore, there is probably a tradeoff between the azimuth of the dike system and that of the western dipping sliding fault below the western flank that they assumed to justify the deformation observed on the western flank. The inconsistency of this western dipping sliding fault with the geophysical and geological knowledge of the volcano is discussed below.

6.2. Deep Plumbing System

[46] In this paper we infer pressurized sources that were active before, during and after the eruption. The effects of these sources are evident on both all the comparisons between GPS surveys and the DInSAR maps considered in this work. The results of our analysis prove that, during and after the eruption, the western flank felt the effects of a

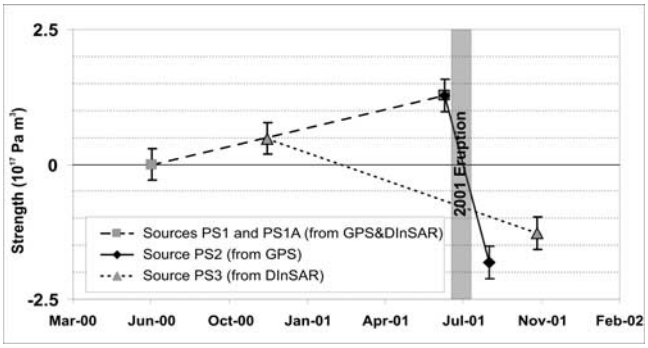

Figure 9. Plot of the strength of the pressure sources found in this study versus time. The names of the sources are the same reported in the Tables 4, 7, and 9. The cumulative strength of the sources PS1 and PS3 is shown to be comparable with the strength of the source PS2 (assuming that the inflation rate from June to October 2000 was the same measured from June 2000 to July 2001).

pressure source located relatively close to the one detected before the eruption onset. Together, these pressure sources (i.e., those active before and during the eruption) could be thought as belonging to a unique pressurized volume used by the magma during its ascent through in the shallow crust. Confirmation of this interpretation comes from the comparison among the "strength" of the sources identified in this study from different data sets. Figure 9, indeed, shows that the evolution in time of the strength of these pressure sources concurs in identifying the evolution of a unique source which pressurized before the eruption and depressurized during and after it. This interpretation also agrees with the hypothesis of a source, independent from the central conduit, feeding the LV of the 2001 (the peripheral dike in *Acocella and Neri* [2003]), and the idea based on gravity data [*Carbone et al.*, 2003], deformation data [*Bonaccorso et al.*, 2004] and petrologic studies [*Métrich et al.*, 2004] that the magma emitted by the LV must have come directly from a deep source.

[47] We note that these sources caused the strong deflation measured by DInSAR on the western flank of the volcano (Figure 7), which was also recognized by *Lundgren and Rosen* [2003]. However, they did not assume any pressure source and modeled the deformations of the western flank by introducing a westward sliding plane to increase the western flank motion away from the SAR sensor in descending images. This model conflicts both with the current geological and geophysical knowledge of Mount Etna, which in no way suggests the presence of such a plane, as well as with the observed data. For instance, it is expected that such a plane should produce an uplift at lower altitudes on the western flank [see *Lundgren and Rosen*, 2003, Figure 4a] not observed on ground deformation patterns of Mount Etna, neither since deformations have been monitored on this volcano (about 25 years) nor on the 2000–2001 GPS and DInSAR data set, as the interferometric residuals confirm (Figure 7d).

[48] In summary, by using GPS and DInSAR, we infer the dynamic of a source that inflated before the eruption and deflated during and after it. This structure is located at about 4–9 km bsl, beneath the upper western flank of the volcano. Although minor differences in the vertical position of the pressure sources before the eruption inferred by using the two surveying techniques (see Table 4), we can suppose that they were either due to the different investigated time interval and/or to the differences in the nature of the data set. During the eruption, the depressurizations seemed to move deeper suggesting that the rapid upward intrusion of the dike induced a magma ascent from depth. This strongly agrees with the petrochemical characteristics of the erupted magma. During the final stage of the eruption, indeed, *Spillaert et al.* [2006] observed that the most primitive products of the eruption had deeper origins than those erupted at the beginning (N. Métrich, personal communication, 2006). Rapid magma uprising was also suggested by *Carbone et al.* [2003] to justify the gravity increase observed close to the LV from 19 July to 2 August 2001. A similar mechanism, which involves depressurization of lower volumes during the magma ascent, was probably anticipated before the eruption during the seismic crisis occurring in April 2001 studied by *Bonaccorso et al.* [2004]. By integrating seismic and geodetic data, they proposed that the uprising of magma from an overpressurized reservoir began in spring, causing a depressurization of the same reservoir that produced a slight temporary lowering of the GPS permanent stations located in the central part of the volcano. It is noteworthy that the pressure sources identified throughout the 2 years encompassing the eruption are located along the western boundary of the HVB (Figure 8); this is a volume of shallow crust that *Patanè et al.* [2003] propose as one of the preferential ways for the magma ascent beneath Mount Etna.

6.3. Implication on Volumes and Medium Properties

[49] Considering that the solidified dike should contain about 20×10^6 m^3 of magma and that the erupted dense rock from the LV is about $22–30 \times 10^6$ m^3, we estimate that at least $42–50 \times 10^6$ m^3 of magma in total flowed out during the eruption from the pressure sources discussed in section 6.2. These data allow us to discuss the consistency of the pressure source models discussed above with the volcanological data. According to *McTigue* [1987] the volume injected in a Mogi-type source (V) is proportional to the ratio between the strength (S) and the rigidity (μ), according to the relation

$$V = S^* \pi / \mu. \quad (1)$$

[50] During the inversion we assumed that $\mu = 30$ GPa, as a bulk rigidity of the crust involved in the deformations. The simple form of equation (1) gives the opportunity to check this value, by investigating the agreement between the corresponding changes in volume within these sources and the volume of magma that left these sources. According to the results of Table 7 and equation (1), the depletion of magma in the source from July to September 2001 should be about 33×10^6 m^3, i.e., 30–40% lower than expected. This suggests that the actual rigidity should range from 20 to 22 GPa, in order to match the estimates of volume changes at the sources with that of the "out-flowed" volume (i.e., $42–50 \times 10^6$ m^3). We can consider this value as an experimental estimation of the bulk "effective rigidity" as intended by *Bonaccorso et al.* [2005]. By applying

this effective rigidity to the results of the source acting from July 2000 to July 2001, i.e., before the eruption, we obtain that the volume of magma injected within the source is about $18-21 \times 10^6$ m^3, thus between 1/3 and 1/2 of the amount involved in the eruption. This means that the eruption involved magma stored even before July 2000, suggesting that the filling of the magmatic system started long before July 2000. Thus the seismic swarms recorded in November 2000, which marks the positive variation of the seismic strain release before the eruption [*Bonaccorso et al.*, 2004], do not represent the beginning of the inflations but rather its effect. The filling process leading to the 2001 eruption could then be considered as a continuation of that producing the inflation of the volcano measured since the end of 1991–1993 eruption [see *Puglisi et al.*, 2004, and references therein].

6.4. Dynamic of the Eastern Flank

[51] Another interesting feature studied in this research is the influence of the dike intrusion on the ground deformation pattern of the eastern flank of the volcano. The subhorizontal plane calculated by inverting the data from the July–September 2001 comparison, confirms the position of the one modeled by *Bonforte and Puglisi* [2003], but it is wider, less dipping and involves the entire flank of the volcano. This geometry is significantly different from that assumed by *Lundgren and Rosen* [2003], who propose a shorter 30° ESE dipping normal fault. The eastern sliding plane we infer is always needed to invert the data (both GPS and DInSAR), in order to fit the stronger displacement measured on the eastern side of the volcano with respect to the western one. The slip rate along this plane is about 3 cm/a before the eruption, which is the same order of magnitude both of the cumulative rate calculated from 1996 to 1998 for the structures on the southeastern flank by *Froger et al.* [2001], using DInSAR data, and the rate calculated from 1997 to 1999 by *Azzaro et al.* [2001] from the GPS network of the Pernicana fault on the northeastern flank. The movement along the decollement accelerated due to the dike intrusion, reaching a value of about 17 cm/a during the eruption. After the end of the eruption, the slip rate dropped to about 10 cm/a from September to October 2001, not even reaching the values measured before the eruption. During the 2001 autumn, the eastern periphery of the volcano released the stress cumulated during the dike intrusion, producing the seismic swarm that struck this area in October. Looking at the displacement vectors of the September–October 2001 comparison (Figure 6), it is possible to note how their magnitude increases from higher to lower stations, contrary to what was measured during the July–September 2001 comparison (Figure 5b).

[52] An interesting detail of the dynamic of the east flank is the local response of the TFS to the volcanic stress field, both before and after the eruption. Before the eruption, the lower eastern flank shows a significant deformation along a narrow NNW-SSE strip (Figure 4a); this feature was probably due to a response of the TFS and SLF to the stress induced by the inflation of the volcano at this time. The easternmost vertical fault (SLF) always shows the most significant dip slip dislocation, with the uplift of the eastern side, according to the compressive stress induced on the volcano periphery by the inflation due to the pressurization of the plumbing system. After the eruption, the western vertical fault (TFS) changes its kinematics with respect to the preeruptive period, showing a significant right-lateral dislocation with a minor dip-slip component, which is in good agreement with the kinematics derived from the focal solutions of the earthquakes occurring in that area in October 2001. This observation confirms that the ground deformation field was propagating downward over the eastern flank of the volcano, allowing the stress accumulated during the dike intrusion to be released.

6.5. Reconstruction of the Eruption

[53] By summarizing all the above discussions, we can propose the following dynamic model of Mount Etna encompassing the 2001 eruption.

[54] Following the same trend of the long-lasting inflation after the end of the 1991–1993 eruption, Mount Etna underwent a year of evident inflation due to the pressurization of the plumbing system at medium depth after June 2000. The magma stocked at about 4–9 km bsl (Tables 4, 7, and 9) within a "storage volume" already inferred from ground deformation data since 1993 [*Puglisi and Bonforte*, 2004; *Bonaccorso et al.*, 2005; *Palano et al.*, 2007] (Figure 10a). The depth and timing inferred from ground deformation data are also compatible with petrochemical studies that proved that the 2001 eruption was triggered by the pressurization of a closed-system dike, located at about 5 km bsl due to the formation of volatiles while the magma rising from depth of about 12 km was crystallizing [*Métrich et al.*, 2004]. The present study backdates the beginning of the filling of the plumbing system with respect to the November 2000 seismic swarm, which marks the increase of the seismic release of the volcano before the eruption [*Bonaccorso et al.*, 2004]. The cumulated volume stored in the year before the eruption onset, indeed, is evaluated between 18 and 20×10^6 m^3, suggesting that the filling of the source started before June 2000.

[55] In February–April 2001 the intrusive process started, as suggested from seismic and deformation data [*Bonaccorso et al.*, 2004], involving a volume of volcanic basement located farther southeast with respect to the deep plumbing system active since this period (Figure 10b). However, according to the modeling of the gravity data proposed by *Carbone et al.* [2003], the top of this magma batch did not rise above 3 km bsl.

[56] On 12 July, the final phase of the intrusion began. In a few days the magna passed through about 4–5 km of basement and volcanic pile. The rapid depressurization of the magma storage due to the process of the dike intrusion between 12 and 15 July induced the magma rising from depth (about 9 km bsl); this facilitated the continuation of this process which produced the emerging of the dike at the volcano surface (Figure 10c).

[57] The eastern flank of the volcano underwent a short-term (in terms of days or weeks) elastic response due to the impulsive compressive stress induced by the very quick dike intrusion. Since the elastic deformations rapidly decrease with distance, we retain that the wall rock continued to exert a compressive stress on the dike during the eruption, as confirmed by the deformation episode occurring on 25 July [*Bonforte et al.*, 2004]. Later on (in terms of weeks or months) the cumulated stress was released, and the

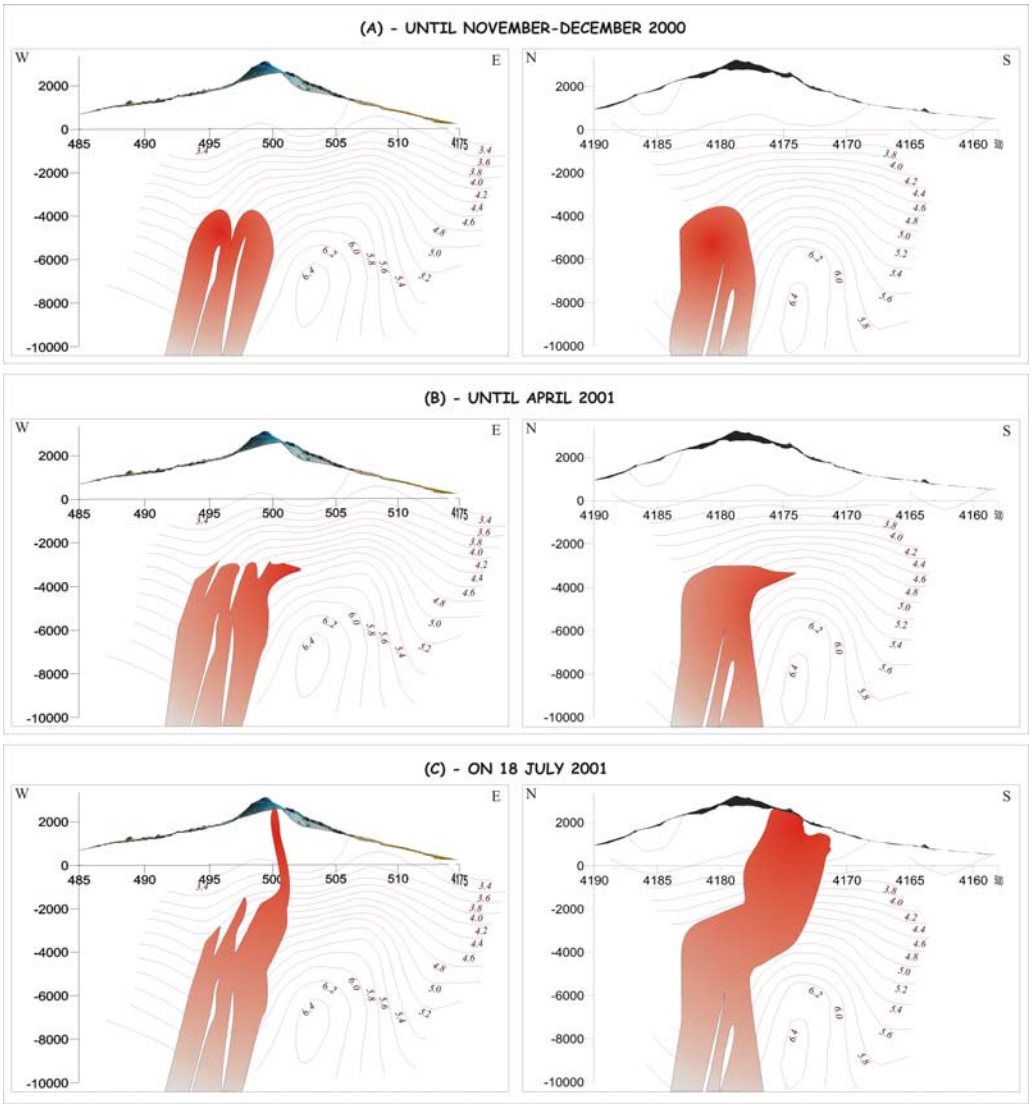

Figure 10. East-west and north-south schematic sections showing three steps of the magma rising: (a) until November–December 2000; (b) until April 2001; (c) on 18 July 2001. The isolines indicate the Vp values resulting from the *Chiarabba et al.* [2000] tomography.

ground deformation propagated to the eastern periphery of the volcano. The propagation started from the upper south-eastern flank, along a NNW-SSE fault near the intrusive dike, as already detected early during the intrusion [*Gambino*, 2004] and during the first days of the eruption by *Bonforte et al.* [2004].

7. Conclusions

[58] In this paper, we take advantage of the favorable circumstances of having GPS and DInSAR deformation data right on time to detect ground deformation related to the 2001 eruption. Particular care has been given to the data processing in order to (1) maintain the same appropriate reference frame for all the five GPS surveys carried out throughout 2000 and 2001 and (2) overcome the problems affecting the ERS-2 gyroscopes at the beginning of 2001. Using GPS and DInSAR data, we are able to identify the volcanic and structural features that played a fundamental role in determining the dynamic of the volcano before, during, and after the 2001 Mount Etna eruption.

[59] During the year preceding the eruption a deep source pressurized beneath the upper western flank of the volcano. This source depressurized during and after the eruption, confirming that the probable source of the magma feeding the lower eruptive system of the 2001 eruption was a ponding zone, at a depth ranging from 9 to 4 km bsl, as proposed by *Métrich et al.* [2004] and *Corsaro et al.* [2006] from petrochemical studies. This conclusion strongly supports the hypothesis that this zone was also pressurizing throughout the 90s (although probably due to different subsequent magma batches), producing the inflations observed by the ground deformation monitoring system [*Bonaccorso and Davis*, 2004; *Puglisi et al.*, 2004]. On the grounds of the volume changes inferred to this source before and after the eruption we suggest that the actual mean values of the bulk "effective rigidity" of medium considered in the models should range from 20 to 22 GPa.

[60] From July to September 2001, the intrusion of the eruptive dike dominates the deformation pattern that shows an almost elastic behavior of the volcanic edifice, with N-S compression and E-W extension, compatible with the regional stress field [*Cocina et al.*, 1997; *Lanzafame et al.*, 1997] and an attenuation of the E-W displacements toward the periphery of the volcano; this induced a strong compressive stress field on the eastern and western peripheries of the volcano. This study allows detailing the dike intrusion in the shallow crust during the days before the opening of LV. The rising of the magma during the last kilometers seems strongly driven by the local stress fields. The westward displacement and the enlargement of the dike as it approached the surface were indeed probably controlled by the topography of the Valle del Bove depression which provokes a rotation of the σ_3. The present study confirms the hypothesis put forward by several studies [e.g., *Acocella and Neri*, 2003; *Bonaccorso et al.*, 2004; *Carbone et al.*, 2003; *Métrich et al.*, 2004] that this dike was fed throughout the eruption by the deep source; the magma uprising from depth was particularly fast at the beginning of the eruption.

[61] The western flank of the volcano, which is buttressed by the Appenine-Maghrebian chain [*Froger et al.*, 2001], maintained its elastic behavior in time, while the eastern one, that faces the Hyblean-Maltese tectonic escarpment, progressively released the stress cumulated, by propagating the deformation far from the intrusion area. This phenomenon caused a sudden acceleration of the sliding of this flank of the volcano that continued after the end of the eruption. This is confirmed, on the southeastern side, by the GPS measurements carried out in October. The acceleration of the sliding also caused a local response of the TFS to the stress induced on the lowermost eastern flank of the volcano, revealed by the seismic activity and GPS measurements.

[62] The ground deformation data analyzed here allowed improving the modeling of the sliding plane beneath the eastern flank of the volcano, detected by *Bonforte and Puglisi* [2003]. The inversions confirmed the location of the previous model, but found a wider plane with a smaller dip angle. The new model reveals how the detachment extends beneath the whole eastern flank of the volcano and how its dip angle decreases eastward. Considering the current slope angle of the volcano edifice, it is reasonable to conceive of the modeled sliding dislocation as a quasi-horizontal plane, which approximates a listric surface beneath the eastern flank of the volcano [*Bonforte and Puglisi*, 2006].

[63] **Acknowledgments.** We thank the two anonymous referees for their reviews that led to substantial improvements with respect to the original version of the manuscript. We thank the Associate Editor, Isabelle Manighetti, for her helpful comments in preparing the final version of the manuscript. We are also grateful to many colleagues for the constructive discussions on this study, particularly A. Bonaccorso, M. Burton, D. Carbone, R. Corsaro, N. Métrich and E. Rivalta. We are deeply indebted to the technical staff of the INGV-CT Ground Deformation Unit, who ensured the regular working of the monitoring networks during the tasking days of the 2001 eruption; in particular, we would like to thank B. Puglisi, M. Cantarero, and O. Consoli. The authors thank M. Mattia for the data of the GPS permanent stations and TRE staff for helpful support in SAR data processing. We also thank S. Conway for correcting and improving the English of this paper. We acknowledge the "Istituto Nazionale di Geofisica e Vulcanologia", the Italian "Dipartimento per la Protezione Civile" and the European Community (contract INGV-DPC UR V3_6/36 and VOLUME Project) for their economic contribution to this research. The SAR data are provided by ESA-ESRIN.

References

Acocella, V., and M. Neri (2003), What makes flank eruptions? The 2001 Etna eruption and its possible triggering smechanisms, *Bull. Volcanol.*, *65*, 517–529, doi:10.1007/s00445-003-0280-3.

Alparone, S., and S. Gambino (2003), High precision locations of multiplets on south-eastern flank of Mt. Etna (Italy): Reconstruction of fault plane geometry, *Phys. Earth Planet. Inter.*, *135*, 281–289, doi:10.1016/S0031-9201(03)00048-7.

Altamimi, Z., P. Sillard, and C. Boucher (2002), ITRF2000: A new release of the International Terrestrial Reference Frame for Earth science applications, *J. Geophys. Res.*, *107*(B10), 2214, doi:10.1029/2001JB000561.

Armienti, P., F. Innocenti, R. Petrini, M. Pompilio, and L. Villari (1989), Petrology and Sr-Nd isotope geochemistry of recent lavas from Mt. Etna: Bearing on the volcano feeding system, *J. Volcanol. Geotherm. Res.*, *39*, 315–327, doi:10.1016/0377-0273(89)90095-4.

Azzaro, R. (1999), Earthquake surface faulting at Mt. Etna volcano (Sicily) and implications for active tectonics, *J. Geod.*, *28*, 193–213, doi:10.1016/S0264-3707(98)00037-4.

Azzaro, R., M. Mattia, and G. Puglisi (2001), Fault creep and kinematics of the eastern segment of the Pernicana fault (Mt. Etna, Sicily) derived from geodetic observations and their tectonic significance, *Tectonophysics*, *333*, 401–415, doi:10.1016/S0040-1951(01)00021-X.

Azzaro, R., S. D'Amico, A. Mostaccio, and L. Scarfì (2002), Terremoti con effetti macrosismici in Sicilia orientale—Calabria meridionale nel periodo Gennaio 1999–Dicembre 2001, *Quad. Geof.*, *27*, 59 pp.

Beauducel, F., P. Briole, and J. L. Froger (2000), Volcano wide fringes in ERS synthetic aperture radar interferograms of Etna (1992–1998): Deformation or tropospheric effect?, *J. Geophys. Res.*, *105*(B7), 16,391–16,402, doi:10.1029/2000JB900095.

Behncke, B., and M. Neri (2003), The July–August 2001 eruption of Mt. Etna (Sicily), *Bull. Volcanol.*, *65*, 461–476, doi:10.1007/s00445-003-0274-1.

Beutler, G., W. Gurtner, M. Rotacher, U. Wild, and E. Frei (1990), Relative static positioning with the Global Positioning System: Basic technical considerations, in *Global Positioning System: An Overview*, edited by Y. Bock and N. Leppard, pp. 1–23, Springer, Berlin, Germany.

Bonaccorso, A., and P. D. Davis (2004), Modeling of ground deformations associated with recent lateral eruptions: Mechanics of magma ascent and intermediate storage at Mt. Etna, in *Mt. Etna: Volcano Laboratory, Geophys. Monogr. Ser.*, vol. 143, edited by A. Bonaccorso et al., pp. 293–306, AGU, Washington, D. C.

Bonaccorso, A., M. Aloisi, and M. Mattia (2002), Dike emplacement forerunning the Etna July 2001 eruption modeled through continuous tilt and GPS data, *Geophys. Res. Lett.*, *29*(13), 1624, doi:10.1029/2001GL014397.

Bonaccorso, A., S. D'Amico, M. Mattia, and D. Patanè (2004), Intrusive mechanism at Mt Etna forerunning the July-August 2001 eruption, *Pure Appl. Geophys.*, *161*(7), 1469–1487, doi:10.1007/s00024-004-2515-4.

Bonaccorso, A., S. Cianetti, C. Giunchi, E. Trasatti, M. Bonafede, and E. Boschi (2005), Analytical and 3-D numerical modelling of Mt. Etna (Italy) volcano inflation, *Geophys. J. Int.*, *163*, 852–862, doi:10.1111/j.1365-246X.2005.02777.x.

Bonaccorso, A., A. Bonforte, F. Guglielmino, M. Palano, and G. Puglisi (2006), Composite ground deformation pattern forerunning the 2004–2005 Mount Etna eruption, *J. Geophys. Res.*, *111*, B12207, doi:10.1029/2005JB004206.

Bonforte, A., and G. Puglisi (2003), Magma uprising and flank dynamics on Mount Etna volcano studied using GPS data (1994–1995), *J. Geophys. Res.*, *108*(83), 2153, doi:10.1029/2002JB001845.

Bonforte, A., and G. Puglisi (2006), Dynamics of the eastern flank of Mt. Etna volcano (Italy) investigated by a dense GPS network, *J. Volcanol. Geotherm. Res.*, *153*, 357–369, doi:10.1016/j.jvolgeores.2005.12.005.

Bonforte, A., F. Guglielmino, M. Palano, and G. Puglisi (2004), A syn-eruptive ground deformation episode measured by GPS, during the 2001 eruption, in the upper southern flank of Mt. Etna, *Bull. Volcanol.*, *66*, 336–341, doi:10.1007/s00445-003-0314-x.

Borgia, A., L. Ferrari, and G. Pasquarè (1992), Importance of gravitational spreading in the tectonic and volcanic evolution of Mount Etna, *Nature*, *357*, 231–235, doi:10.1038/357231a0.

Bousquet, J. C., and G. Lanzafame (2004), The tectonics and geodynamics of Mt. Etna: synthesis and interpretation of geological and geophysical data, in *Mt. Etna: Volcano Laboratory, Geophys. Monogr. Ser.* vol. 143, edited by A. Bonaccorso et al., pp. 29–47, AGU, Washington, D. C.

Carbone, D., G. Budetta, and F. Greco (2003), Bulk processes prior the 2001 Mount Etna eruption, highlighted through microgravity studies, *J. Geophys. Res.*, *108*(B12), 2556, doi:10.1029/2003JB002542.

Chiarabba, C., A. Amato, E. Boschi, and F. Barberi (2000), Recent seismicity and tomographic modeling of the Mount Etna plumbing system, *J. Geophys. Res.*, *105*(B5), 10,923–10,938, doi:10.1029/1999JB900427.

Chiarabba, C., P. De Gori, and D. Patanè (2004), The Mt. Etna plumbing system: The contribution of seismic tomography, in *Mt. Etna: Volcano Laboratory, Geophys. Monogr. Ser.*, vol. 143, edited by A. Bonaccorso et al., pp. 191–204, AGU, Washington, D.C.

Cocina, O., G. Neri, E. Privitera, and S. Spampinato (1997), Stress tensor computations in the Mount Etna area (southern Italy) and tectonic implications, *J. Geodyn.*, *23*, 109–127, doi:10.1016/S0264-3707(96)00027-0.

Coltelli, M., P. Del Carlo, and S. Scollo (2001), Physical parameters of the ash fallout occurred during the 2001 eruption of Etna and implication for volcanic hazard assessment, paper presented at 1st year GNV-INGV Assembly, Rome, 9–11 Oct.

Coltelli, M., C. Proietti, S. Branca, M. Marsella, D. Andronico, and L. Lodato (2007), Analysis of the 2001 lava flow eruption of Mt. Etna from three-dimensional mapping, *J. Geophys. Res.*, *112*, F02029, doi:10.1029/2006JF000598.

Corsaro, R. A., and M. Pompilio (2004), Dynamics of magmas at Mount Etna, in *Mt. Etna: Volcano Laboratory, Geophys. Monogr. Ser.*, vol. 143, edited by A. Bonaccorso et al., pp. 91–*110*, AGU, Washington, D. C.

Corsaro, R. A., L. Miraglia, and M. Pompilio (2006), Petrologic evidence of a complex plumbing system feeding the July-August 2001 eruption of Mt. Etna, Sicily, Italy, *Bull. Volcanol.*, *69*(4), 401–421, doi:10.1007/s00445-006-0083-4.

Dahm, T. (2000), Numerical simulations of the propagation path and the arrest of fluid-filled fractures in the Earth, *Geophys. J. Int.*, *141*, 623–638, doi:10.1046/j.1365-246x.2000.00102.x.

Falsaperla, S., S. Alparone, S. D'Amico, G. Di Grazia, F. Ferrari, H. Langer, T. Sgroi, and S. Spampinato (2005), Volcanic tremor at Mt. Etna, Italy, preceding and accompanying the eruption of July-August 2001, *Pure Appl. Geophys.*, *162*, 2111–2132, doi:10.1007/s00024-005-2710-y.

Froger, J. L., O. Merle, and P. Briole (2001), Active spreading and regional extension at Mount Etna imaged by SAR interferometry, *Earth Planet Sci. Lett.*, *187*, 245–258, doi:10.1016/S0012-821X(01)00290-4.

Gambino, S. (2004), Continuous dynamic response along a pre-existing structural discontinuity induced by the 2001 eruption at Mt. Etna, *Earth Planets Space*, *56*, 447–456.

Gresta, S., V. Longo, and A. Viavattene (1990), Geodynamic behaviour of eastern and western sides of Mt. Etna, *Tectonophysics*, *179*, 81–92, doi:10.1016/0040-1951(90)90357-E.

INGV Staff (2001), Multidisciplinary approach yields insight into Mt. Etna eruption, *Eos Trans. American Geophysical Union*, *82*(52), 653.

Lanzafame, G., and J. C. Bousquet (1997), The Maltese escarpment and its extension from Mt. Etna to the Aeolian islands (Sicily): Importance and evolution of a lithosphere discontinuity, *Acta Vulcanol.*, *9*, 113–120.

Lanzafame, G., M. Neri, and D. Rust (1996), A preliminary structural evaluation of recent tectonic activity on the eastern flank of Mount Etna, Sicily, *West London Pap. Environ. Stud.*, *3*, 73–90.

Lanzafame, G., M. Neri, M. Coltelli, L. Lodato, and D. Rust (1997), North-South compression in the Mt. Etna region (Sicily): Spatial and temporal distribution, *Acta Vulcanol.*, *9*, 121–133.

LoGiudice, E., and R. Rasà (1992), Very shallow earthquakes and brittle deformations in active volcanic areas: The Etnean region as an example, *Tectonophysics*, *202*, 257–268, doi:10.1016/0040-1951(92)90111-I.

Lundgren, P., and A. Rosen (2003), Source model for the 2001 flank eruption of Mt. Etna volcano, *Geophys. Res. Lett.*, *30*(7), 1388, doi:10.1029/2002GL016774.

Martinez-Arevalo, C., D. Patané, A. Rietbrock, and J. M. Ibanez (2005), The intrusive process leading to the Mt. Etna 2001 flank eruption: Constraints from 3-D attenuation tomography, *Geophys. Res. Lett.*, *32*, L21309, doi:10.1029/2005GL023736.

Massonnet, D., and K. Feigl (1998), Radar interferometry and its application to changes in the Earth's surface, *Rev. Geophys.*, *36*, 441–500, doi:10.1029/97RG03139.

McGuire, W. J. (1989), Simulating active volcanoes, *Geol. Today*, *5*, 93–96, doi:10.1111/j.1365-2451.1989.tb00631.x.

McTigue, F. D. (1987), Elastic stress and deformation near a finite spherical magma body: Resolution of the point source paradox, *J. Geophys. Res.*, *92*(B12), 12931–12,940, doi:10.1029/JB092iB12p12931.

Métrich, N., P. Allard, N. Spilliaert, D. Andronico, and M. Burton (2004), 2001 flank eruption of the alkali- and volatile-rich primitive basalt responsible for Mount Etna's evolution in the last three decades, *Earth Planet. Sci. Lett.*, *228*, 1–17, doi:10.1016/j.epsl.2004.09.036.

Mogi, K. (1958), Relation between the eruptions of various volcanoes and the deformations of the ground surfaces around them, *Bull. Earthquake Res. Inst. Univ. Tokyo*, *36*, 99–134.

Nunnari, G., G. Puglisi, and S. R. Maugeri (1995), An optimisation approach for the inversion of the ground deformation data, in *Proceedings of the Workshop New Challenges for Geodesy in Volcanic Monitoring*, Walferdange–Luxembourg June 14–16, 1993, *Cah. Centre Eur. Geodyn. Seismol.*, *8*, 329–348.

Palano, M., G. Puglisi, and S. Gresta (2007), Ground deformation patterns at Mt. Etna from 1993 to 2000 from joint use of InSAR and GPS techniques, *J. Volcanol. Geotherm. Res.*, *169*(3), 99–120, doi:10.1016/j.jvolgeores.2007.08.014.

Patane, D., C. Chiarabba, O. Cocina, P. De Gori, M. Moretti, and E. Boschi (2002), Tomographic images and 3D earthquake locations of the seismic swarm preceding the 2001 Mt. Etna eruption: Evidence for a dyke intrusion, *Geophys. Res. Lett.*, *29*(10), 1497, doi:10.1029/2001GL014391.

Patanè, D., P. De Gori, C. Chiarabba, and A. Bonaccorso (2003), Magma ascent and the pressurization of Mount Etna's volcanic system, *Science*, *299*, 2061, doi:10.1126/science.1080653.

Puglisi, G., and A. Bonforte (2004), Dynamics of Mount Etna Volcano inferred from static and kinematic GPS measurements, *J. Geophys. Res.*, *109*, B11404, doi:10.1029/2003JB002878.

Puglisi, G., P. Briole, and A. Bonforte (2004), Twelve years of ground deformation studies on Mt. Etna volcano based on GPS surveys, in *Mt. Etna: Volcano Laboratory, Geophys. Monogr. Ser.*, vol. 143, edited by A. Bonaccorso et al., pp. 321–341, AGU, Washington, D. C.

Rasà, R., R. Azzaro, and O. Leonardi (1996), Aseismic creep on faults and flank instability at Mt. Etna volcano, in *Volcano Instability on the Earth and Other Planets*, edited by W. J. McGuire, A. P. Jones, J. Neuberg, *Geol. Soc. Spec. Publ.*, *110*, 179–192.

Rust, D., and M. Neri (1996), The boundaries of large-scale collapse on the flanks of Mount Etna, Sicily, in *Volcano Instability on the Earth and Other Planets*, edited by W. J. McGuire, A. P. Jones, J. Neuberg, *Geol. Soc. Spec. Publ.*, *110*, 193–208.

Rust, D., B. Behncke, M. Neri, and A. Ciocanel (2005), Nested zones of instability in the Mount Etna volcanic edifice, Sicily, *J. Volcanol. Geotherm. Res.*, *144*, 137–153, doi:10.1016/j.jvolgeores.2004.11.021.

Spilliaert, N., P. Allard, N. Métrich, and A. V. Sobolev (2006), Melt inclusion record of the conditions of ascent, degassing, and extrusion of volatile-rich alkali basalt during the powerful 2002 flank eruption of Mount Etna (Italy), *J. Geophys. Res.*, *111*, B04203, doi:10.1029/2005JB003934.

Taddeucci, J., M. Pompilio, and P. Scarlato (2002), Monitoring the explosive activity of the July–August 2001 eruption of Mt. Etna (Italy) by ash characterization, *Geophys. Res. Lett.*, *29*(8), 1230, doi:10.1029/2001GL014372.

A. Bonforte, F. Guglielmino, M. Palano, and G. Puglisi, Istituto Nazionale di Geofisica e Vulcanologia, Sezione di Catania, Piazza Roma, 2, I-95123 Catania, Italy. (puglisi-g@ct.ingv.it)

A. Ferretti, Tele-Rilevamento Europa s.r.l., via Vittoria Colonna, 7, I-20149 Milano, Italy.

C. Prati, POLIMI-DEI, Piazza Leonardo da Vinci, 32, I-20133 Milano, Italy.